Evaluation of global terrestrial evapotranspiration by state-of-the-art approaches in remote sensing, machine learning, and land surface modeling

Shufen Pan[1], Naiqing Pan[1,2], Hanqin Tian[1], Pierre Friedlingstein[3], Stephen Sitch[4], Hao Shi[1],

Vivek K. Arora[5], Vanessa Haverd[6], Atul K. Jain[7], Etsushi Kato[8], Sebastian Lienert[9], Danica

Lombardozzi[10], Julia E.M.S. Nabel[11], Catherine Ottlé[12], Benjamin Poulter[13,], Sönke Zaehle[14],

Steven W. Running[15]

[1]International Center for Climate and Global Change Research, School of Forestry and Wildlife

Sciences, Auburn University, Auburn, AL 36832, USA

[2]State Key Laboratory of Urban and Regional Ecology, Research Center for Eco-Environmental

Sciences, Chinese Academy of Sciences, Beijing 100085, China

[3]College of Engineering, Mathematics and Physical Sciences, University of Exeter, Exeter EX4

4QF, United Kingdom

[4]College of Life and Environmental Sciences, University of Exeter, Exeter EX4 4RJ, United

Kingdom

[5]Canadian Centre for Climate Modelling and Analysis, Environment Canada, University of

Victoria, Victoria, BC, Canada

[6]CSIRO Oceans and Atmosphere, GPO Box 1700, Canberra, ACT 2601, Australia

[7]Department of Atmospheric Sciences, University of Illinois, Urbana, IL 61801, USA

[8]Institute of Applied Energy (IAE), Minato-ku, Tokyo 105-0003, Japan

[9]Climate and Environmental Physics, Physics Institute, University of Bern, Bern, Switzerland

[10]Climate and Global Dynamics Laboratory, National Center for Atmospheric Research,

Boulder, CO 80305, USA

[11]Max Planck Institute for Meteorology, Bundesstr. 53, 20146 Hamburg, Germany

24   [12]LSCE-IPSL-CNRS, Orme des Merisiers, 91191, Gif-sur-Yvette, France

25   [13]NASA Goddard Space Flight Center, Biospheric Science Laboratory, Greenbelt, MD 20771,

26   USA

27   [14]Max Planck Institute for Biogeochemistry, P.O. Box 600164, Hans-Knöll-Str. 10, 07745 Jena,

28   Germany

29   [15]Numerical Terradynamic Simulation Group, College of Forestry & Conservation, University of

30   Montana, Missoula, MT 59812, USA

32   ***Corresponding author**: panshuf@auburn.edu, Tel: 1-334-844-1015

33   **Abstract**

34   Evapotranspiration (ET) is critical in linking global water, carbon and energy cycles. Yet direct

35   measurement of global terrestrial ET is not feasible. Here, we first reviewed the basic theory and

36   state-of-the-art approaches for estimating global terrestrial ET, including remote sensing-based

37   physical models, machine learning algorithms and land surface models (LSMs). We then utilized

38   four remote sensing-based physical models, two machine-learning algorithms and fourteen LSMs

39   to analyze the spatial and temporal variations in global terrestrial ET. The results showed that the

40   ensemble means of annual global terrestrial ET estimated by these three categories of approaches

41   agreed well, ranging from 589.6 mm yr^{-1} (6.56×10^4 km^3 yr^{-1}) to 617.1 mm yr^{-1} (6.87×10^4 km^3 yr^{-1}

42   ). For the period 1982-2011, both the ensembles of remote sensing-based physical models and

43   machine-learning algorithms suggested increasing trends in global terrestrial ET (0.62 mm yr^{-2} ,

44    $p<0.05$ and 0.38 mm yr^{-2} , $p<0.05$, respectively). In contrast, the ensemble mean of LSMs showed

45   no statistically significant change (0.23 mm yr^{-2}, $p>0.05$), even though many of the individual

46   LSMs reproduced an increasing trend. Nevertheless, all the twenty models used in this study

47 showed anthropogenic Earth greening had a positive role in increasing terrestrial ET. The

48 concurrent small inter-annual variability, i.e. relative stability, found in all estimates of global

49 terrestrial ET, suggests there exists a potential planetary boundary in regulating global terrestrial

50 ET, with the value being around 600 mm yr^{-1}. Uncertainties among approaches were identified in

51 specific regions, particularly in the Amazon Basin and arid/semi-arid regions. Improvements in

52 parameterizing water stress and canopy dynamics, utilization of new available satellite retrievals

53 and deep learning methods, and model-data fusion will advance our predictive understanding of

54 global terrestrial ET.

55

56 **Keywords**: Evapotranspiration; Land surface models; Remote sensing; Machine learning.

57

1. Introduction

59 Terrestrial evapotranspiration (ET) is the sum of the water loss to the atmosphere from plant tissues

60 via transpiration and that from the land surface elements including soil, plants and open water

61 bodies through evaporation. Processes controlling ET play a central role in linking the energy

62 (latent heat), water (moisture flux), and carbon cycles (photosynthesis-transpiration trade-off) in

63 the earth system. Over 60% of precipitation on the land surface is returned to the atmosphere

64 through ET (Oki and Kanae, 2006), and the accompanying latent heat (λET, λ is the latent heat of

65 vaporization) accounts for more than half of the solar energy received by the land surface

66 (Trenberth et al., 2009). ET is also coupled with the carbon dioxide exchange between canopy and

67 atmosphere through vegetation photosynthesis. These linkages make ET an important variable in

68 both the short-term numerical weather forecast and long-term climate prediction. Moreover, ET is

69 a critical indicator for ecosystem functioning across a variety of spatial scales. For enhancing our

70 predictive understanding of earth system and sustainability, therefore, it is essential to accurately

71 assess land surface ET in a changing global environment.

72 However, large uncertainty still exists in quantifying the magnitude of global terrestrial ET and its

73 spatial and temporal patterns, despite extensive research (Allen et al., 1998; Liu et al., 2008;

74 Miralles et al., 2016; Mueller et al., 2011; Tian et al., 2010). The previous estimates of global land

75 mean annual ET range from 417 mm yr^{-1} to 650 mm yr^{-1} for the whole or part of the 1982-2011

76 period (Mu et al., 2007; Mueller et al., 2011; Vinukollu et al., 2011a; Zhang et al., 2010). This

77 large discrepancy among independent studies may be attributed to lack of sufficient measurements,

78 uncertainty in forcing data, inconsistent spatial and temporal resolutions, ill-calibrated model

79 parameters and deficiencies in model structures. Of the four components of ET (transpiration, soil

80 evaporation, canopy interception, and open-water evaporation), transpiration (T_v) contributes the

81 largest uncertainty, as it is modulated not only by surface meteorological conditions and soil

82 moisture but also by the physiology and structures of plants. Changes in non-climatic factors such

83 as elevated atmospheric CO_2, nitrogen deposition, and land covers also serve as influential drivers

84 of T_v (Gedney et al., 2006; Mao et al., 2015; Pan et al., 2018b; Piao et al., 2010). As such, the

85 global ratio of transpiration to ET (T_v/ET) has long been of debate, with the most recent

86 observation-based estimate being 0.64±0.13 constrained by the global water-isotope budget (Good

87 et al., 2015). Most earth system models are thought to largely underestimate T_v/ET (Lian et al.,

88 2018).

89 Global warming is expected to accelerate the hydrological cycle (Pan et al., 2015). For the period,

90 1982 to the late 1990s, ET was reported to increase by about 7 mm (~1.2%) per decade driven by

91 an increase in radiative forcing and consequently global and regional temperatures (Douville et al.,

92 2013; Jung et al., 2010; Wang et al., 2010). The contemporary near-surface specific humidity also

93   increased over both land and ocean (Dai, 2006; Simmons et al., 2010; Willett et al., 2007). More

94   recent studies confirmed that, since the 1980s, global ET has showed an overall increase (Mao et

95   al., 2015; Yao et al., 2016; Zeng et al., 2018a; Zeng et al., 2012; Zeng et al., 2016; Zhang et al.,

96   2015; Zhang et al., 2016b). However, the magnitude and spatial distribution of such a trend are far

97   from determined. Over the past 50 years, pan evaporation decreased throughout the world (Fu et

98   al., 2009; Peterson et al., 1995; Roderick and Farquhar, 2002), implying an increase in actual ET

99   given the pan evaporation paradox. Moreover, the increase in global terrestrial ET was found to

100   cease or even be reversed during 1998 to 2008, primarily due to the decreased soil moisture supply

101   in the Southern Hemisphere (Jung et al., 2010). To reconcile the disparity, Douville et al. (2013)

102   argued that the peak ET in 1998 should not be taken as a tipping point because ET was estimated

103   to increase in the multi-decadal evolution. More efforts are needed to understand the spatial and

104   temporal variations of global terrestrial ET and the underlying mechanisms that control its

105   magnitude and variability.

106   Conventional techniques, such as lysimeter, eddy covariance, large aperture scintillometer and the

107   Bowen ratio method, are capable of providing ET measurements at point and local scales (Wang

108   and Dickinson, 2012). However, it is impossible to directly measure ET at the global scale because

109   dense global coverage by such instruments is not feasible and the representativeness of point-scale

110   measurements to comprehensively represent the spatial heterogeneity of global land surface is also

111   doubtful (Mueller et al., 2011). To address this issue, numerous approaches have been proposed

112   in recent years to estimate global terrestrial ET and these approaches can be divided into three

113   main categories: 1) remote sensing-based physical models, 2) machine learning algorithms, and 3)

114   land surface models (Miralles et al., 2011; Mueller et al., 2011; Wang and Dickinson, 2012).

115   Knowledge of the uncertainties in global terrestrial ET estimates from different approaches is the

116 prerequisite for future projection and many other applications. In recent years, several studies have

117 compared multiple terrestrial ET estimates (Khan et al., 2018; Mueller et al., 2013; Wartenburger

118 et al., 2018; Zhang et al., 2016b). However, most of these studies analyzed multiple datasets of the

119 same approach or focused on investigating similarities and differences among different

120 approaches. Few studies have been conducted to identify uncertainties in multiple estimates of

121 different approaches.

122 In this study, we integrate state-of-the-art estimates of global terrestrial ET, including data-driven

123 and process-based estimates, to assess its spatial pattern, inter-annual variability, environmental

124 drivers, long-term trend, and response to vegetation greening. Our goal is not to compare the

125 various models and choose the best one, but to identify the uncertainty sources in each type of

126 estimate and provide suggestions for future model development. In the following sections, we first

127 have a brief introduction to all methodological approaches and ET datasets used in this study. We

128 then quantify the spatiotemporal variations in global terrestrial ET during the period 1982-2011

129 by analyzing the results from the current state-of-the-art models. Finally, we discuss some

130 suggested solutions for reducing the identified uncertainties.

131 **2. Methodology and data sources**

132 **2.1 Overview of approaches to global ET estimation**

133 **2.1.1 Remote sensing-based physical models**

134 Satellite remote sensing has been widely recognized as a promising tool to estimate global ET,

135 because it is capable of providing spatially and temporally continuous measurements of critical

136 biophysical parameters affecting ET, including vegetation states, albedo, fraction of absorbed

137 photosynthetically active radiation, land surface temperature and plant functional types (Li et al.,

138 2009). Since the 1980s, a large number of methods have been developed using a variety of satellite

139 observations (Zhang et al., 2016a). However, part of these methods such as surface energy balance

140 (SEB) models and surface temperature-vegetation index (Ts-VI) are usually applied at local and

141 regional scales. At the global scales, the vast majority of existing remote sensing-based physical

142 models can be categorized into two groups: the Penman-Monteith (PM) based and the Priestley-

143 Taylor (PT) based models.

144 A) Remote sensing models based on Penman-Monteith equation

145 The Penman equation, derived from the Monin-Obukhov similarity theory and surface energy

146 balance, uses surface net radiation, temperature, humidity, wind speed and ground heat flux to

147 estimate ET from an open water surface. For vegetated surfaces, canopy resistance was introduced

148 into the Penman equation by Monteith (Monteith, 1965) and the PM equation is formulated as:

149
$$\lambda \text{ET} = \frac{\Delta(R_n - G) + \rho_a C_p VPD / r_a}{\Delta + \gamma(1 + {r_s}/{r_a})} \tag{1}$$

150 where Δ, R_n, G, ρ_a, C_p, γ, r_s, r_a, VPD are the slope of the curve relating saturated water vapor

151 pressure to air temperature, net radiation, soil heat flux, air density, the specific heat of air,

152 psychrometric constant, surface resistance, aerodynamic resistance and vapor pressure deficit,

153 respectively. The canopy resistance term in the PM equation exerts a strong control on

154 transpiration. For example, based on the algorithm proposed by Cleugh et al. (2007), the MODIS

155 (Moderate Resolution Imaging Spectroradiometer) ET algorithm improved the model performance

156 through inclusion of environmental stress into canopy conductance calculation and explicitly

157 accounted for soil evaporation (Mu et al., 2007). Further, Mu et al. (2011) improved the MODIS

158 ET algorithm by considering nighttime ET, adding soil heat flux calculation, separating dry canopy

159 surface from the wet, and dividing soil surface into saturated wet surface and moist surface.

160 Similarly, Zhang et al. (2010) developed a Jarvis-Stewart-type canopy conductance model based

161 on normalized difference vegetation index (NDVI) to take advantage of the long-term Advanced

162   Very High Resolution Radiometer (AVHRR) dataset. More recently, this model was improved by

163   adding a CO_2 constraint function in the canopy conductance estimate (Zhang et al., 2015). Another

164   important revision for the PM approach is proposed by Leuning et al. (2008). The Penman-

165   Monteith-Leuning method adopts a simple biophysical model for canopy conductance, which can

166   account for influences of radiation and atmospheric humidity deficit. Additionally, it introduces a

167   simpler soil evaporation algorithm than that proposed by Mu et al. (2007), which potentially makes

168   it attractive to use with remote sensing. However, PM-based models have one intrinsic weakness:

169   temporal upscaling which is required in translating instantaneous ET estimation into a longer time-

170   scale value (Li et al., 2009).This could be easily done at the daily scale under clear-sky conditions

171   but faces challenge at weekly to monthly time-scales due to lack of cloud coverage information.

172   B) Remote sensing models based on Priestley-Taylor equation

173   The Priestley–Taylor (PT) equation is a simplification of the PM equation without parameterizing

174   aerodynamic and surface conductance (Priestley and Taylor, 1972) and can be expressed as:

175   $$\lambda\text{ET} = f_{stress} \times \alpha \times \frac{\Delta}{\Delta+\gamma} \times (R_n - G) \qquad (2)$$

176   where f_{stress} is a stress factor and is usually computed as a function of environmental conditions. α

177   is the PT parameter with a value of 1.2–1.3 under water unstressed conditions and can be estimated

178   using remote sensing. Although the original PT equation works well in estimating potential ET

179   across most surfaces, the Priestley-Taylor coefficient, α, usually needs adjustment to convert

180   potential ET to actual ET (Zhang et al., 2016a). Instead, Fisher et al. (2008) developed a modified

181   PT model that keeps α constant but scales down potential ET by ecophysiological constraints and

182   soil evaporation partitioning. The accuracy of their model has been validated against eddy

183   covariance measurements conducted at a wide range of climates and plant functional types (Fisher

184   et al., 2009; Vinukollu et al., 2011b). Following this idea, Yao et al. (2013) further developed a

185 modified Priestley-Taylor algorithm that constrains soil evaporation using the Apparent Thermal

186 Inertia derived index of soil water deficit. Miralles et al. (2011) also proposed a novel PT type

187 model, Global Land surface Evaporation: the Amsterdam Methodology (GLEAM). GLEAM

188 combines a soil water module, a canopy interception model and a stress module within the PT

189 equation. The key distinguishing features of this model are the use of microwave-derived soil

190 moisture, land surface temperature and vegetation density, and the detailed estimation of rainfall

191 interception loss. In this way, GLEAM minimizes the dependence on static variables, avoids the

192 need for parameter tuning, and enables the quality of the evaporation estimates to rely on the

193 accuracy of the satellite inputs (Miralles et al., 2011). Compared with the PM approach, the PT

194 based approaches avoid the computational complexities of aerodynamic resistance and the

195 accompanying error propagation. However, the many simplifications and semi-empirical

196 parameterization of physical processes in the PT based approaches may lower its accuracy.

197 **2.1.2 Vegetation index-based empirical algorithms and machine learning methods**

198 The principle of empirical ET algorithms is to link observed ET to its controlling environmental

199 factors through various statistical regressions or machine learning algorithms of different

200 complexities. The earliest empirical regression method was proposed by Jackson et al. (1977). At

201 present, the majority of regression models are based on vegetation indices (Glenn et al., 2010),

202 such as NDVI and enhanced vegetation index (EVI), because of their simplicity, resilience in the

203 presence of data gaps, utility under a wide range of conditions and connection with vegetation

204 transpiration capacity (Maselli et al., 2014; Nagler et al., 2005; Yuan et al., 2010). As an alternative

205 to statistical regression methods, machine learning algorithms have been gaining increased

206 attention for ET estimation due to their ability to capture the complex nonlinear relationships

207 between ET and its controlling factors (Dou and Yang, 2018). Many conventional machine

208 learning algorithms, such as artificial neural networks, random forest, and support vector machine

209 based algorithms have been applied in various ecosystems (Antonopoulos et al., 2016; Chen et al.,

210 2014; Feng et al., 2017; Shrestha and Shukla, 2015) and have proved to be more accurate in

211 estimating ET than simple regression models (Antonopoulos et al., 2016; Chen et al., 2014; Kisi

212 et al., 2015; Shrestha and Shukla, 2015; Tabari et al., 2013). In up-scaling FLUXNET ET to the

213 global scale, Jung et al. (2010) used the model tree ensemble method to integrate eddy covariance

214 measurements of ET with satellite remote sensing and surface meteorological data. In a recent

215 study (Bodesheim et al., 2018), the random forest approach was used to derive global ET at a half-

216 hourly time-scale.

217 **2.1.3 Process-based land surface models (LSMs)**

218 Although satellite-derived ET products have provided quantitative investigations of historical

219 terrestrial ET dynamics, they can only cover a limited temporal record of about four decades. To

220 obtain terrestrial ET before 1980s and predict future ET dynamics, LSMs are needed, as they are

221 able to represent a large number of interactions and feedbacks between physical, biological, and

222 biogeochemical processes in a prognostic way (Jimenez et al., 2011). ET simulation in LSMs is

223 regulated by multiple biophysical and physiological properties or processes, including but not

224 limited to stomatal conductance, leaf area, root water uptake, soil water, runoff and sometimes

225 nutrient uptake (Famiglietti and Wood, 1991; Huang et al., 2016; Lawrence et al., 2007). Although

226 almost all current LSMs have these components, different parameterization schemes result in

227 substantial differences in ET estimation (Wartenburger et al., 2018). Therefore, in recent years,

228 the multi-model ensemble approach has become popular in quantifying magnitude, spatiotemporal

229 pattern and uncertainty of global terrestrial ET (Mueller et al., 2011; Wartenburger et al., 2018).

230 Yao et al. (2017) showed that a simple model averaging method or a Bayesian model averaging

231 method is superior to each individual model in predicting terrestrial ET.

2.2 Description of ET models used in this study

233 In this study, we evaluate twenty ET products that are based on remote sensing-based physical

234 models, machine-learning algorithms, and LSMs to investigate the magnitudes and spatial patterns

235 of global terrestrial ET over recent decades. Table 1 lists the input data, adopted ET algorithms,

236 limitations, and references for each product. We use a simple model averaging method when

237 calculating the mean value of multiple models.

238 Four physically-based remote sensing datasets, including Process-based Land Surface

239 Evapotranspiration/Heat Fluxes algorithm (P-LSH), Global Land surface Evaporation: the

240 Amsterdam Methodology (GLEAM), Moderate Resolution Imaging Spectroradiometer (MODIS)

241 and PML-CSIRO (Penman-Monteith-Leuning), and two machine-learning datasets, including

242 Random Forest (RF) and Model Tree Ensemble (MTE), are used in our study. Both machine

243 learning and physical-based remote sensing datasets (totally six datasets) were considered as

244 benchmark products. The ensemble mean of benchmark products was calculated as the mean value

245 of all machine learning and physical-based satellite estimates since we treated each benchmark

246 dataset equally.

247 Three of the four remote sensing-based physical models quantify ET through PM approaches. P-

248 LSH adopts a modified PM approach coupling with biome-specific canopy conductance

249 determined from NDVI (Zhang et al., 2010). The modified P-LSH model used in this study also

250 accounts for the influences of atmospheric CO_2 concentrations and wind speed on canopy stomatal

251 conductance and aerodynamic conductance (Zhang et al., 2015). MODIS ET model is based on

252 the algorithm proposed by Cleugh et al. (2007). Mu et al. (2007) improved the model performance

253 through the inclusion of environmental stress into canopy conductance calculation, and explicitly

254 accounting for soil evaporation by combing complementary relationship hypothesis with PM

255 equation. The MODIS ET product (MOD16A3) used in this study was further improved by

256 considering night-time ET, simplifying vegetation cover fraction calculation, adding soil heat flux

257 item, dividing saturated wet and moist soil, separating dry and wet canopy, as well as modifying

258 algorithms of aerodynamic resistance, stomatal conductance, and boundary layer resistance (Mu

259 et al., 2011). PML-CSIRO adopts the Penman-Monteith-Leuning algorithm, which calculates

260 surface conductance and canopy conductance by a biophysical model instead of classic empirical

261 models. The maximum stomatal conductance is estimated using the trial-and-error method (Zhang

262 et al., 2016b). Furthermore, for each grid covered by natural vegetation, the PML-CSIRO model

263 constrains ET at the annual scale using the Budyko hydrometeorological model proposed by Fu

264 (1981). GLEAM ET calculation is based on the PT equation, which requires fewer model inputs

265 than PM equation, and the majority of these inputs can be directly achieved from satellite

266 observations. Its rationale is to make the most of information about evaporation contained in the

267 satellite-based environmental and climatic observations (Martens et al., 2017; Miralles et al.,

268 2011). Key variables including air temperature, land surface temperature, precipitation, soil

269 moisture, vegetation optical depth and snow-water equivalent are satellite-observed. Moreover,

270 the extensive usage of microwave remote sensing products in GLEAM ensures the accurate

271 estimation of ET under diverse weather conditions. Here, we use the GLEAM v3.2 version which

272 has overall better quality than previous version (Martens et al., 2017).

273 The first used machine learning model, MTE, is based on the Tree Induction Algorithm (TRIAL)

274 and Evolving Trees with Random Growth (ERROR) algorithm (Jung et al., 2009). The TRIAL

275 grows model trees from the root node and splits at each node with the criterion of minimizing the

276   sum of squared errors of multiple regressions in both subdomains. ERROR is used to select the

277   model trees that are independent from each other and have best performances under Schwarz

278   criterion. Canopy fraction of absorbed photosynthetic active radiation (fAPAR), temperatures,

279   precipitation, relative humidity, sunshine hours, and potential radiation are used as explanatory

280   variables to train MTE (Jung et al., 2011). The second machine learning model is the random forest

281   (RF) algorithm whose rationale is generating a set of independent regression trees through

282   randomly selecting training samples automatically (Breiman, 2001). Each regression tree is

283   constructed using samples selected by bootstrap sampling method. After fixing individual tree in

284   entity, the final result is determined by simple averaging. One merit of RF algorithm is its

285   capability of handling complicated nonlinear problems and high dimensional data (Xu et al., 2018).

286   For the RF product used in this study, multiple explanatory variables including enhanced

287   vegetation index, fAPAR, leaf area index, daytime and nighttime land surface temperature,

288   incoming radiation, top of atmosphere potential radiation, index of water availability and relative

289   humidity were used to train regression trees (Bodesheim et al., 2018).

290   The fourteen LSMs-derived ET products were from the Trends and Drivers of the Regional Scale

291   Sources and Sinks of Carbon Dioxide (TRENDY) Project (including CABLE, CLASS-CTEM,

292   CLM45, DLEM, ISAM, JSBACH, JULES, LPJ-GUESS, LPJ-wsl, LPX-Bern, O-CN,

293   ORCHIDEE, ORCHIDEE-MICT and VISIT). Daily gridded meteorological reanalyses from the

294   CRU-NCEPv8 dataset (temperature, precipitation, long- and short-wave incoming radiation, wind-

295   speed, humidity, air pressure) were used to drive the LSMs. The TRENDY simulations were

296   performed in year 2017 and contributed to the Global Carbon Budget reported in Le Quéré et al.

297   (2018). We used the results of S3 experiment of TRENDYv6 (with changing CO_2, climate and

298 land use) over the period 1982-2011, a time period consistent with other products derived from

299 remote sensing-based physical models and machine-learning algorithms.

2.3 Description of other datasets

301 To quantify the contributions of vegetation greening to terrestrial ET variations, we used the LAI

302 of TRENDYv6 S3 experiment. We also used the newest version of the Global Inventory Modeling

303 and Mapping Studies LAI data (GIMMS LAI3gV1) as satellite-derived LAI. GIMMS LAI3gV1

304 was generated from AVHRR GIMMS NDVI3g using an Artificial Neural Network (ANN) derived

305 model (Zhu et al., 2013). It covers the period 1982 to 2016 with bimonthly frequency and has a

306 1/12° spatial resolution. To achieve a uniform resolution, all data were resampled to 1/2° using the

307 nearest neighbour method. Following Pan et al. (2018a), grids with an annual mean NDVI<0.1

308 were assumed to be non-vegetated regions and were therefore masked out. NDVI data are from

309 GIMMS NDVI3gV1 dataset. Temperature, precipitation and radiation are from CRU-NCEPv8.

2.4 Statistical analysis

311 The significance of ET trends is analyzed using the Mann-Kendall (MK) test (Kendall, 1955;

312 Mann, 1945). It is a rank-based non-parametric method that has been widely applied for detecting

313 a trend in hydro-climatic time series (Sayemuzzaman and Jha, 2014; Yue et al., 2002). The Theil-

314 Sen estimator was applied to estimate the magnitude of the slope. The advantage of this method

315 over ordinary least squares estimator is that it limits the influence of the outliers on the slope (Sen,

316 1968).

317 Terrestrial ET IAV is mainly controlled by variations in temperature, precipitation, and shortwave

318 solar radiation (Zeng et al., 2018b; Zhang et al., 2015). In this study, we performed partial

319 correlation analyses between ET and these three climatic variables at an annual scale for each grid

320   cell to explore climatic controls on ET IAV. Variability caused by climatic variables was assessed

321   through the square of partial correlation coefficients between ET and temperature, precipitation,

322   and radiation. We chose partial correlation analysis because it can quantify the linkage between

323   ET and a single environmental driving factor while controlling the effects of other remaining

324   environmental factors. Partial correlation analysis is a widely applied statistical tool to isolate the

325   relationship between two variables from the confounding effects of many correlated variables

326   (Anav et al., 2015; Jung et al., 2017; Peng et al., 2013). All variables were first detrended in the

327   statistical correlation analysis since we focus on the inter-annual relationship. The study period is

328   from 1982 to 2011 for all models except MODIS and Rand Forest whose temporal coverage is

329   limited to 2001-2011 because of data availability.

330   To quantify the contribution of vegetation greening to terrestrial ET, we separated the trend in

331   terrestrial ET into four components induced by climatic variables and vegetation dynamics by

332   establishing a multiple linear regression model between global ET and temperature, precipitation,

333   shortwave radiation, and LAI (Eq. 3-4):

334
$$\delta(ET) = \frac{\partial(ET)}{\partial(LAI)}\delta(LAI) + \frac{\partial(ET)}{\partial T}\delta(T) + \frac{\partial(ET)}{\partial(P)}\delta(P) + \frac{\partial(ET)}{\partial R}\delta(R) + \varepsilon \qquad (3)$$

335
$$\delta(ET) = \gamma_{ET}^{LAI}\delta LAI + \gamma_{ET}^{T}\delta T + \gamma_{ET}^{P}\delta P + +\gamma_{ET}^{R}\delta R + \varepsilon \qquad (4)$$

336   γ_{ET}^{LAI}, γ_{ET}^{T}, γ_{ET}^{P}, γ_{ET}^{R} are the sensitivities of ET to leaf area index (LAI), air temperature (T),

337   precipitation (P), and radiation (R), respectively. ε is the residual, representing the impacts of other

338   factors.

339   After calculating γ_{ET}^{LAI}, γ_{ET}^{T}, γ_{ET}^{P}, γ_{ET}^{R}, the contribution of trend in factor i ($Trend(i)$) to the trend

340   in ET ($Trend(ET)$) can be quantified as follows:

341
$$\text{Contri(i)} = (\gamma_{ET}^{i} \times Trend(i))/Trend(ET) \qquad (5)$$

342 In performing multiple linear regression, we used GIMMS LAI for both remote sensing-based

343 physical models and machine learning methods, and individual TRENDYv6 LAI for each

344 TRENDY model. The gridded data of temperature, precipitation and radiation are from CRU-

345 NCEPv8

346 **3. Results**

347 **3.1 The ET magnitude estimated by multiple models**
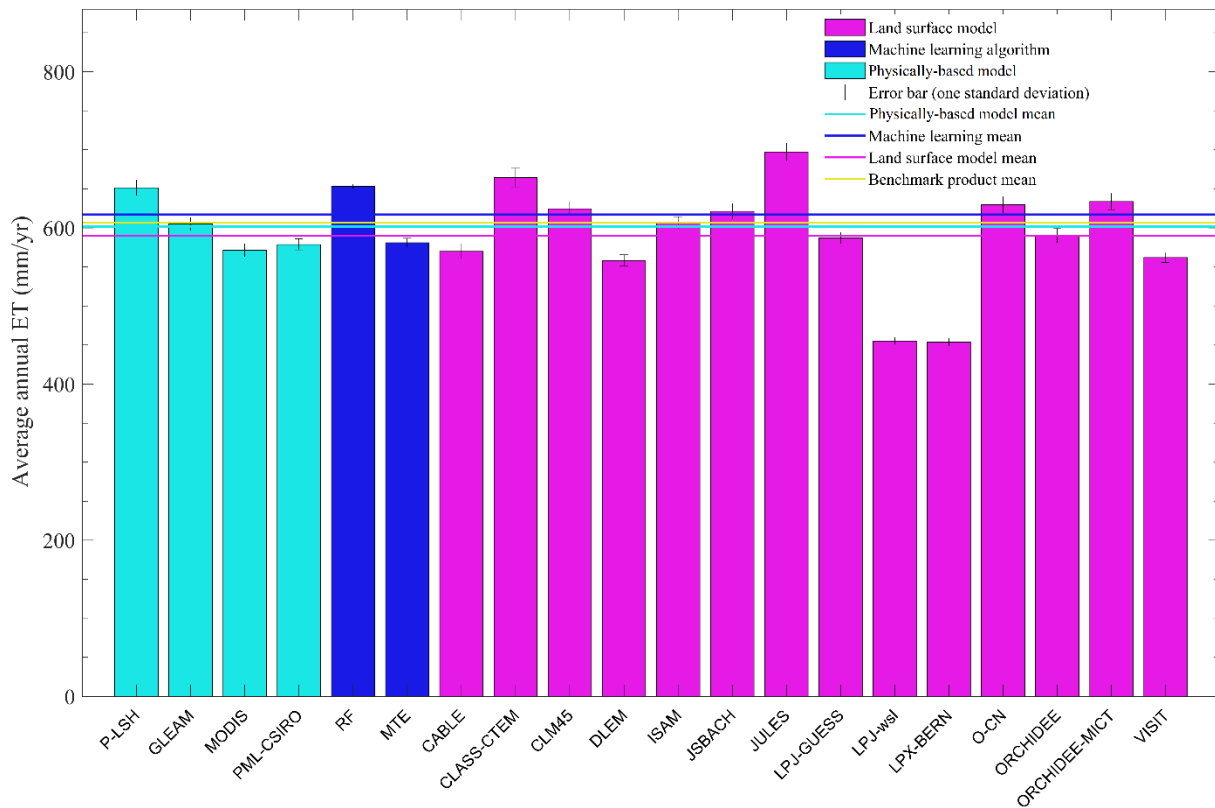
348

349 **Figure 1.** Average annual global terrestrial ET estimated by each model during the period 2001-

350 2011. Error bars represent the standard deviation of each model. The four lines indicate the mean

351 value of each category.

352 The multi-year ensemble mean of annual global terrestrial ET during 2001-2011 derived by the

353 machine learning methods, remote sensing-based physical models and TRENDY models agreed

354 well, ranging from 589.6 mm yr^{-1} to 617.1 mm yr^{-1}. However, substantial differences existed

355 among individual models (Fig. 1). LPJ-wsl (455.3 mm yr^{-1}) and LPX-Bern (453.7 mm yr^{-1})

356 estimated significantly lower ET than other models, even in comparison with most previous studies

357 focusing on earlier periods (Table S1). In contrary, JULES gave the largest ET estimate (697.3

358 mm yr^{-1}, equals to 7.57×10^4 km^3 yr^{-1}) among all models, and showed an obvious increase of ET

359 compared to its estimation during 1950-2000 (6.5×10^4 km^3 yr^{-1}, Table S1).

360 **3.2 Spatial patterns of global terrestrial ET**

361 As shown in Fig. 2, the spatial patterns of multi-year average annual ET of different categories

362 were similar. ET was the highest in the tropics and low in northern high latitudes and arid regions

363 such as Australia, central Asia, western U.S., and Sahel. Compared to remote sensing-based

364 physical models and LSMs, machine-learning methods obtained a smaller spatial gradient. In

365 general, latitudinal profiles of ET estimated by different approaches were also consistent (Fig. 3).

366 However, machine-learning methods gave higher ET estimate at high latitudes and lower ET in

367 the tropics compared to other approaches. In the tropics, LSMs have significant larger uncertainties

368 than benchmark products, and the standard deviation of LSMs is about two times as large as that

369 of benchmark products (Fig. 3). In other latitudes, LSMs and benchmark ET products have

370 generally comparable uncertainties. The largest difference in ET of different categories was found

371 in the Amazon Basin (Fig. 2). In most regions of the Amazon Basin, the mean ET of remote sensing

372 physical models are more than 200mm yr^{-1} higher than the mean ET of LSMs and machine-

373 learning methods. For individual ET estimates, the largest uncertainty was also found in the

374 Amazon Basin. MODIS, VISIT and CLASS-CTEM estimated that annual ET was larger than 1300

375 mm in the majority of Amazon, whereas JSBACH and LPJ-wsl estimated ET of smaller than 800

376 mm yr^{-1} (Fig. S1). As is shown in Fig. S2, the difference in ET estimates among TRENDY models

377 were larger than those among benchmark estimates for tropical and humid regions. The uncertainty

378 of ET estimates by LSMs is particularly large in the Amazon Basin where the standard deviation

379 of LSMs estimates is more than two times as large as that of benchmark estimates. It is noteworthy

380 that, in arid and semi-arid regions such as western Australia, central Asia, northern China and

381 western US, the difference in ET estimates among LSMs is significantly smaller than those among

382 remote sensing models and machine learning algorithms.
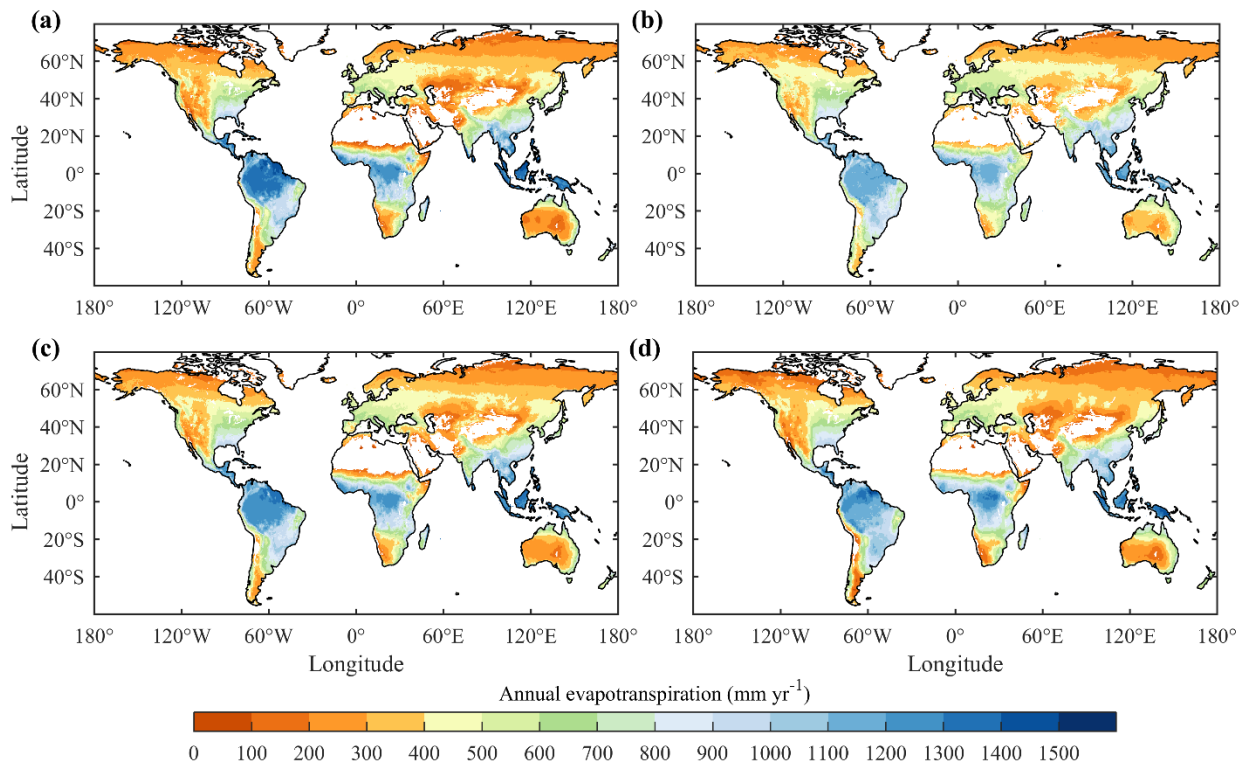
384 **Figure 2.** Spatial distributions of mean annual ET derived from (a) remote sensing-based physical

385 models, (b) machine-learning algorithms, (c) benchmark datasets and (d) TRENDY LSMs

386 ensemble mean, respectively.

387
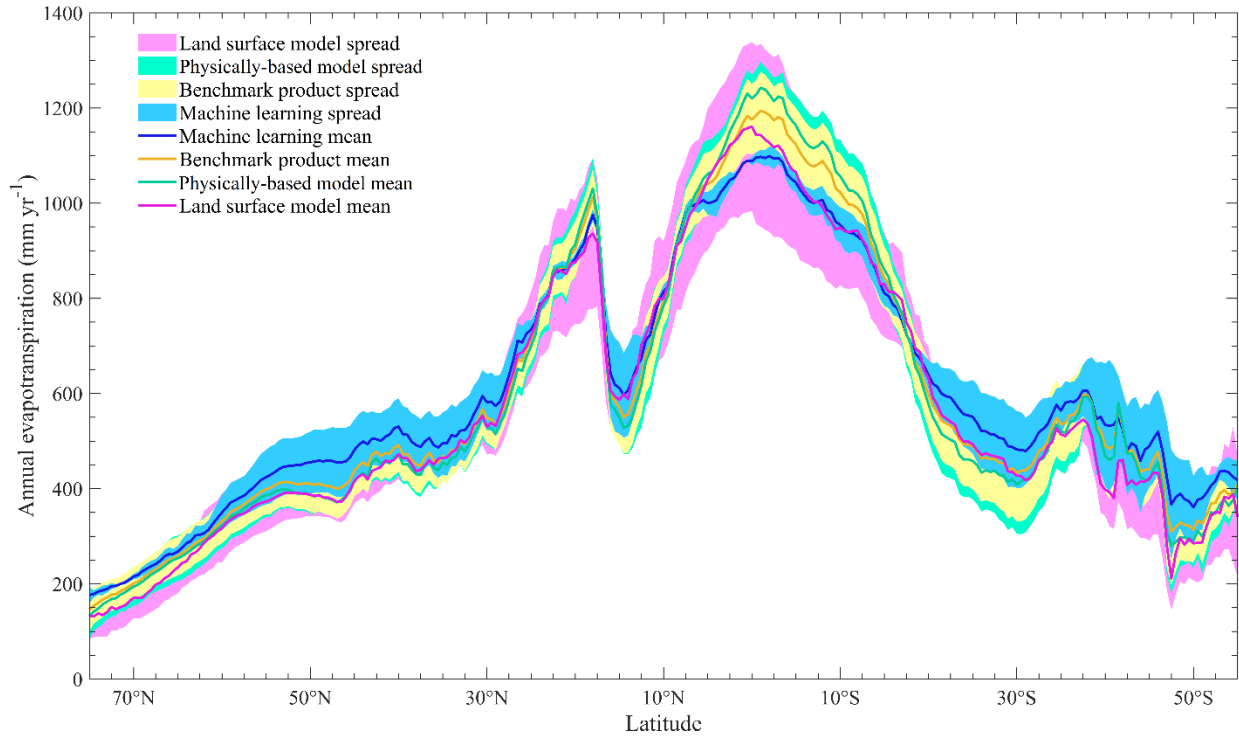
Figure 3. Latitudinal profiles of mean annual ET for different categories of models. Each line

represents the mean value of the corresponding category and the shading represents the interval of

one standard deviation.

3.3 Inter-annual variations in global terrestrial ET

The ensemble mean inter-annual variability (IAV) of remote sensing ET estimates and LSMs ET

estimates showed similar spatial patterns (Fig. 4). Both remote sensing physical models and LSMs

presented low IAV in ET in northern high latitudes but high IAV in ET in southwestern U.S, India,

south Sahara Africa, Amazon and Australia. In contrast, IAV of machine-learning based ET was

much weaker. In most regions, IAV of machine learning ET is smaller than 40% of IAV of remote

sensing physical ET and LSMs ET, and this phenomenon is especially pronounced in tropical

regions. Further investigation into the spatial patterns of ET IAV for individual model showed that

the two machine-learning methods performed equally in estimating spatial patterns of ET IAV

400 (Fig. S4). In contrast, differences in ET IAV among remote sensing physical estimates and LSMs

401 estimates were much larger. LSMs showed the largest differences in IAV of ET in tropical regions.

402 For example, CABLE and JULES obtained an ET IAV of smaller than 15 mm yr^{-1} in most regions

403 of the Amazon Basin, while LPJ-GUESS predicted an ET IAV of larger than 60 mm yr^{-1}. Figure

404 5 showed that, in the north of 20ºS, remote sensing physical ET and LSMs ET had comparable

405 IAV, but IAV of the machine learning based ET was much smaller. In the region south of 20ºS,

406 TRENDY ET showed the largest IAV, followed by those of remote sensing physical ET and

407 machine learning estimates. The three approaches agreed on that ET IAV in the Southern

408 Hemisphere was generally larger than that in the Northern Hemisphere.
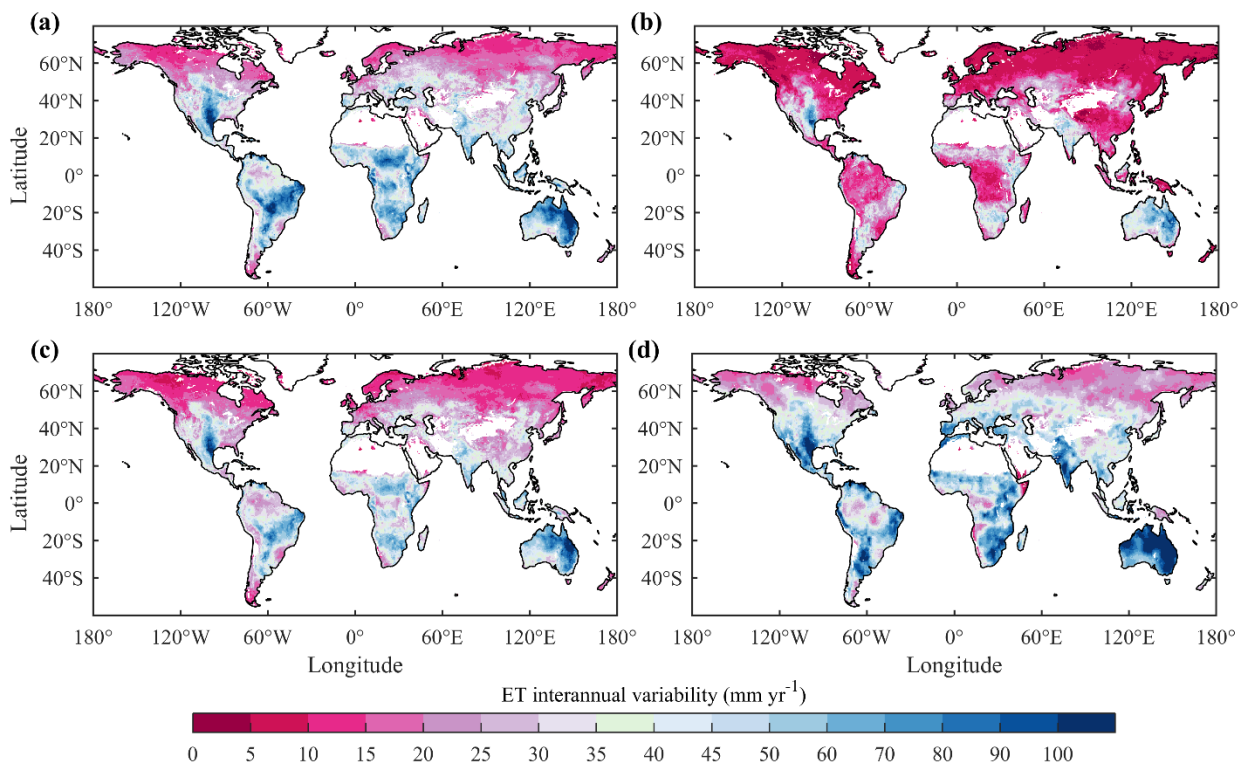
409

410 **Figure 4.** Spatial distributions of the inter-annual variability in ET derived from (a) remote

411 sensing-based physical models, (b) machine learning algorithms, (c) benchmark datasets, and (d)

412   TRENDY LSMs ensemble mean, respectively. The study period used in this study for inter-annual

413   variability analysis is from 1982 to 2011.

414
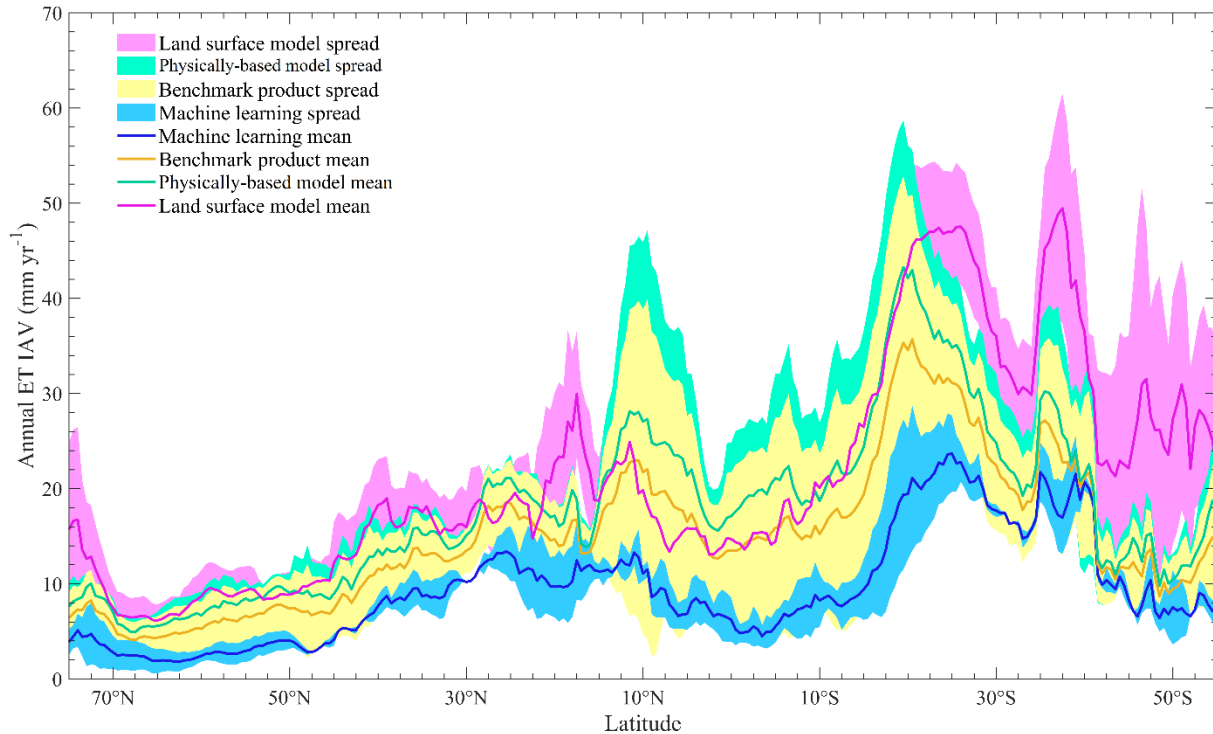
Figure 5. Latitudinal profiles of ET IAV for different categories of models. Each line represents
the mean value of the corresponding category and the shading represents the interval of one
standard deviation.

3.4 Climatic controls on ET

According to the ensemble remote sensing models, temperature and radiation dominated ET IAV
in northern Eurasia, northern and eastern North America, southern China, the Congo River Basin
and the southern Amazon River Basin, while precipitation dominated ET IAV in arid regions and
semi-arid regions (Fig. 6a). The ensemble machine-learning algorithms had a similar pattern, but
suggested a stronger control of radiation in the Amazon Basin and a weaker control of precipitation

424   in several arid regions such as central Asia and northern Australia (Fig. 6b). In comparison, the

425   ensemble LSMs suggested the strongest control of precipitation on ET IAV (Fig. 6). According to

426   the ensemble LSMs, ET IAV was dominated by precipitation IAV in most regions of the Southern

427   Hemisphere and northern low latitudes. Temperature and radiation only controlled northern

428   Eurasia, eastern Canada and part of the Amazon Basin (Fig. 6d). As is shown in Fig. S6, the

429   majority of LSMs agreed on the dominant role of precipitation in controlling ET in regions south

430   of 40ºN. However, the pattern of climatic controls in the ORCHIDEE-MICT model is quite unique

431   and different from all other LSMs. According to the ORCHIDEE-MICT model, radiation and

432   temperature dominate ET IAVs in more regions, and precipitation only controls ET IAVs in

433   eastern Brazil, northern Russia, central Europe and a part of tropical Africa. Since ORCHIDEE-

434   MICT was developed from ORCHIDEE, the dynamic root parameterization in ORCHIDEE-MICT

435   may explain why ET is less driven by precipitation compared to ORCHIDEE (Haverd et al., 2018).

436   It is noted that two machine learning algorithms MTE and RF had significant discrepancies in the

437   spatial pattern of dominant climatic factors. According to the result of MTE, temperature

438   controlled ET IAV in regions north of 45ºN, eastern US, southern China and the Amazon basin

439   (Fig. S6e). By contrast, RF suggested that precipitation and radiation dominated ET IAV in these

440   regions (Fig. S6f).

441
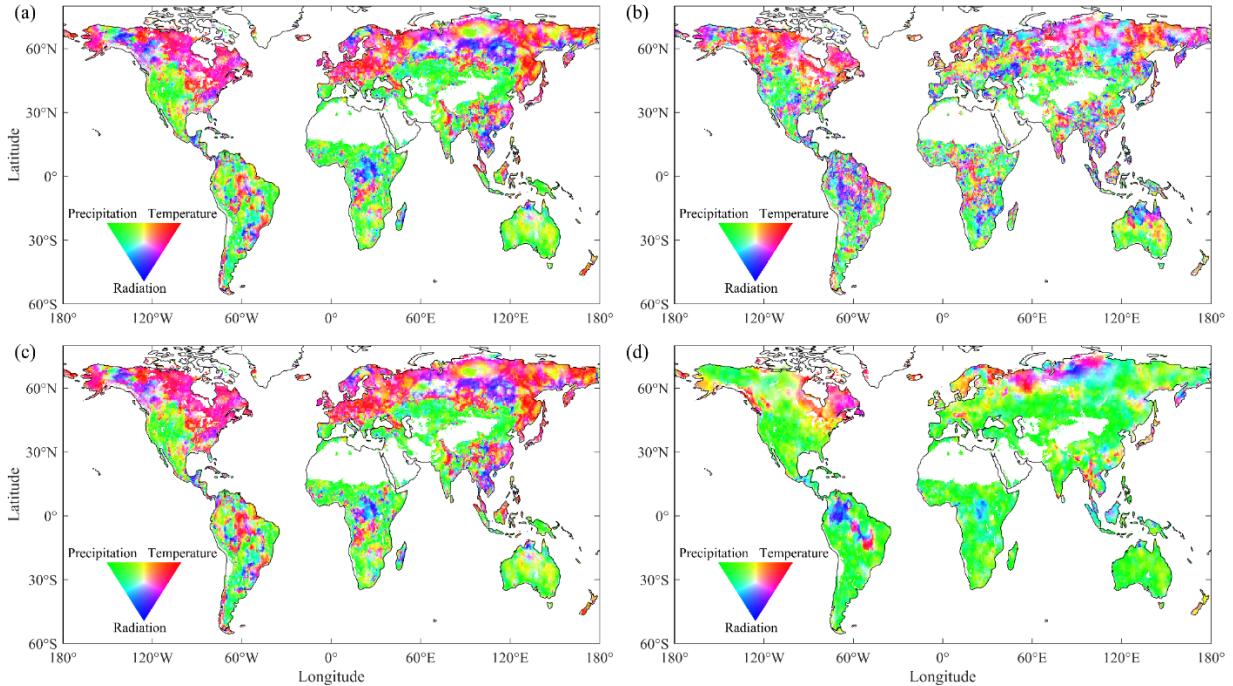
Figure 6. Spatial distributions of climatic controls on inter-annual variation of ET derived from the ensemble means of remote sensing-based physical models (a), machine learning algorithms (b), benchmark data (c), and TRENDY LSMs (d). (red: temperature; green: precipitation; and blue: radiation).

3.5 Long-term trends in global terrestrial ET

All approaches suggested an overall increasing trend in global ET during the period 1982-2011 (Fig. 7), although ET decreased over 1998-2009. This result is consistent with previous studies (Jung et al., 2010; Lian et al., 2018; Zhang et al., 2015). Remote sensing physical models indicated the largest increase in ET (0.62 mm yr^{-2}), followed by the machine-learning method (0.38 mm yr^{-2}), and land surface models (0.23 mm yr^{-2}). Mean ET of all categories except LSMs significantly increased during the study period ($p<0.05$). It is noted that the ensemble mean ET of different categories are statistically correlated with each other ($p<0.001$), even if the driving forces of different ET approaches are different.

456
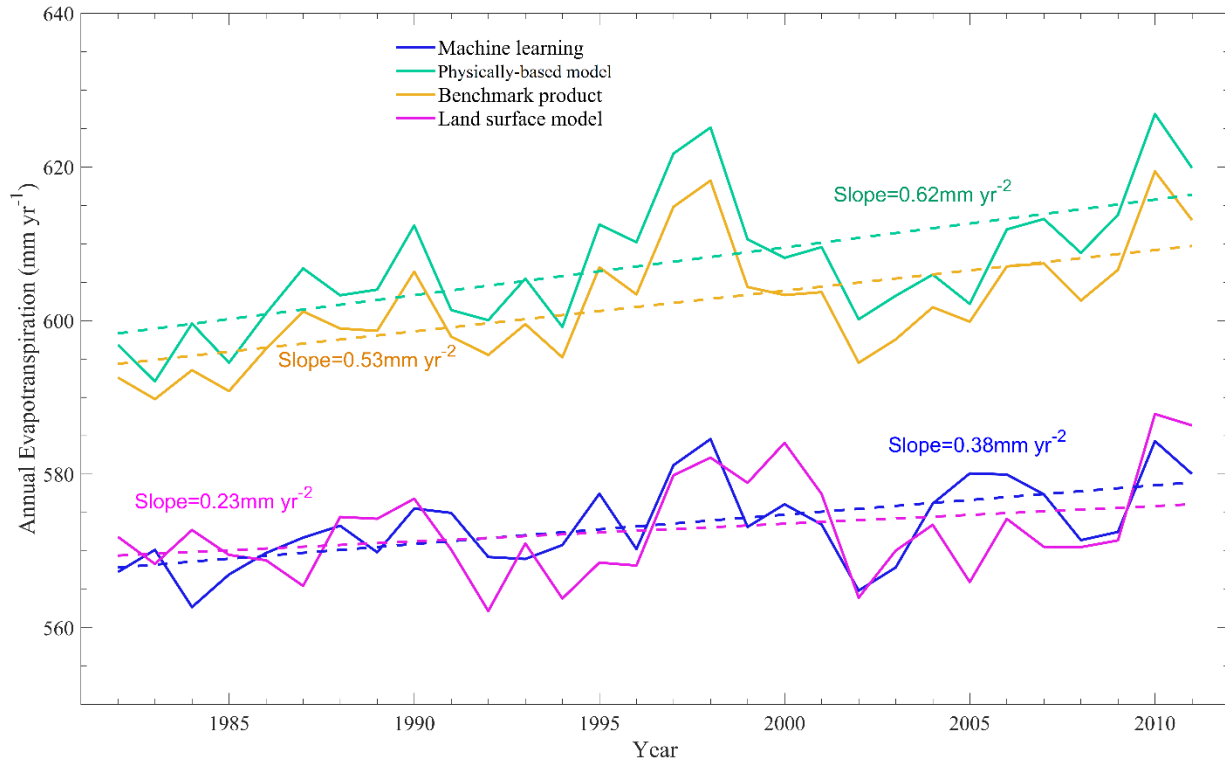
Figure 7. Inter-annual variations in global terrestrial ET estimated by different categories of
approaches.

All remote sensing and machine learning estimates indicate a significant increasing trend in ET
during the study period ($p<0.05$), although the increase rate of P-LSH (1.07 mm yr^{-2}) is more than
three times as large as that of GLEAM (0.33 mm yr^{-2}). Nevertheless, there is a larger discrepancy
among LSMs in terms of ET trend. The majority of LSMs (10 of 14) suggest an increasing trend
with the average trend of 0.34 mm yr^{-2} ($p<0.05$), and eight of them are statistically significant (see
Table 2). However, four LSMs (JSBACH, JULES, ORCHIDEE and ORCHIDEE-MICT) suggest
a decreasing trend with the average trend of -0.12 mm yr^{-2} ($p>0.05$). Among the four decreasing
trends, only the trend of ORCHIDEE-MICT (-0.34 mm yr^{-2}) is statistically significant ($p<0.05$).

467 According to Fig. 8, the ensemble means of all the three approaches showed increasing trends of

468 ET over western and southern Africa, western Indian, and northern Australia, and decreasing ET

469 over western United States, southern South America and Mongolia. Discrepancies in ET trends

470 mainly appeared in East Europe, eastern India and central China. LSMs also suggested larger area

471 of decreasing ET in both North America and South America. Although the differences in ET trends

472 among individual models were larger than those among the ensemble means of different

473 approaches, the majority of models agreed that ET increased in western and southern Africa, and

474 decreased in western United States and southern South America (Fig. S2). For both remote sensing

475 estimates and LSMs estimates, ET trends in Amazon Basin had large uncertainty. P-LSH, CLM-

476 45 and VISIT suggested large area of increasing ET, in contrast, GLEAM, JSBACH and

477 ORCHIDEE suggested a large area of decreasing ET.
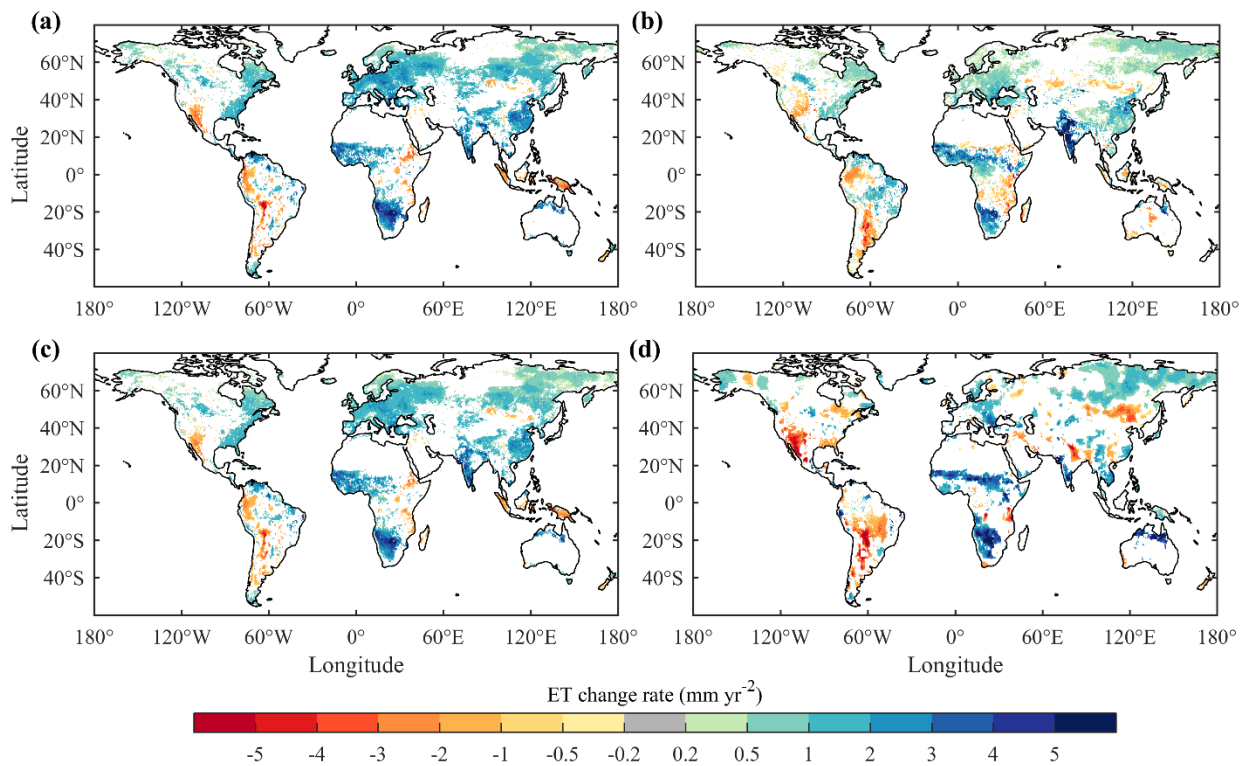
478

479   **Figure 8.** Spatial distributions of ET trends during the period 1982-2011 derived from (a) remote

480   sensing-based physical models, (b) machine learning algorithm, (c) benchmark datasets, and (d)

481   TRENDY LSMs ensemble mean, respectively. Regions with non-significant trends were

482   excluded.

483   **3.6 Impacts of vegetation changes on ET variations**

484   During the period 1982-2011, global LAI trends estimated from remote sensing data and from the

485   ensemble LSMs are 2.51×10^{-3} m^2 m^{-2} yr^{-1} (p<0.01) and 4.63×10^{-3} m^2 m^{-2} yr^{-1} (p<0.01), respectively

486   (Table 2). All LSMs suggested a significant increasing trend in global LAI (greening). It was found

487   that, for both benchmark estimates and LSMs estimates, the spatial pattern of trends in ET matched

488   well with that of trends in LAI (Fig. 8c-d and Fig. S5a-b), indicating significant effects of

489   vegetation dynamics on ET variations. According to the results of multiple linear regression, all

490   models agreed that greening of the Earth since the early 1980s intensified terrestrial ET (Table 2),

491   although there was a significant discrepancy in the magnitude of ET intensification which varied

492   from 0.04 mm yr^{-2} to 0.70 mm yr^{-2}. The ensemble LSMs suggested a smaller ET increase (0.23 mm

493   yr^{-2}) than the ensemble remote sensing physical models (0.62 mm yr^{-2}) and machine-learning

494   algorithm (0.38 mm yr^{-2}). Nevertheless, the greening-induced ET intensification estimated by

495   LSMs (0.37 mm yr^{-2}) is larger than that estimated by remote sensing models (0.28 mm yr^{-2}) and

496   machine-learning algorithms (0.09 mm yr^{-2}) because LSMs suggested a stronger greening trend

497   than remote sensing models. The contribution of vegetation greening to ET intensification

498   estimated by the ensemble LSMs is larger than 100% while the contributions estimated by the

499   ensemble remote sensing physical models (0.62 mm yr^{-2}) and machine-learning algorithm are

500   smaller than 50%. Although TRENDY LSMs were driven by the same climate data and remote

501   sensing physical models were driven by varied climate data, TRENDY LSMs still showed a larger

502 discrepancy in terms of the effect of vegetation greening on terrestrial ET than remote sensing

503 physical models because of the significant differences in both LAI trends ($1.74\text{-}13.63 \times 10^{-3}$ m^2 m^{-2} yr^{-1}) and the sensitivities of ET to LAI ($4.04\text{-}217.39$ mm yr^{-2} per m^2 m^{-2}). In comparison, remote

504 ^{2} yr^{-1}) and the sensitivities of ET to LAI ($4.04\text{-}217.39$ mm yr^{-2} per m^2 m^{-2}). In comparison, remote

505 sensing physical models had smaller discrepancies in terms of the sensitivity of ET to LAI (55.78-

506 143.43 mm yr^{-2} per m^2 m^{-2}).

4. Discussion and perspectives

4.1 Sources of uncertainty

4.1.1 Uncertainty in the ET estimation of Amazon Basin

510 LSMs show large discrepancies in the magnitude and trend of ET in the Amazon Basin (Fig. 3 and

511 Fig. S3). However, it is challenging to identify the uncertainty sources. Given that the TRENDY

512 LSMs used uniform meteorological inputs, the discrepancies in ET estimates among the

513 participating models mainly arise from the differences in underlying model structures and

514 parameters. One potential source of uncertainty is the parameterization of root water uptake. In the

515 Amazon Basin, large root depth was confirmed by field measurements (Nepstad et al., 2004).

516 However, many LSMs have an unrealistically small rooting depth (generally less than 2 m),

517 neglecting the existence and significance of deep roots. The incorrect root distributions enlarge the

518 differences in plant available water and root water uptake, producing large uncertainties in ET. In

519 addition, differences in the parameterization of other key processes pertinent to ET such as LAI

520 dynamics (Fig. S5), canopy conductance variations (Table 1), water movements in the soil

521 (Abramopoulos et al., 1988; Clark et al., 2015; Noilhan and Mahfouf, 1996) and soil moisture's

522 control on transpiration (Purdy et al., 2018; Szutu and Papuga, 2019) also increase the uncertainty

523 in ET. The above-mentioned processes are not independent of each other but interact in complex

524 ways to produce the end result.

4.1.2 Uncertainty in the ET estimation of arid and semi-arid regions

In arid and semi-arid regions, benchmark products show much larger differences in the magnitude of ET than LSMs (Fig. S2). One cause of this phenomenon is the difference in meteorological forcing. Remote sensing and machine learning datasets used different forcing data. For precipitation, RF used the CRUNCEPv6 dataset, MTE used the Global Precipitation Climatology Centre (GPCC) dataset, MODIS used the Global Modeling and Assimilation Office (GMAO) dataset, GLEAM used the Multi-Source Weighted-Ensemble Precipitation (MSWEP) dataset, PML-CSIRO used the Princeton Global Forcing (PGF) and the WATCH Forcing Data ERA-Interim (WFDEI) datasets, and P-LSH used data derived from four independent sources. Since precipitation is the key climatic factor controlling ET in arid and semi-arid regions (Fig. 6), discrepancies between different forcing precipitation (Sun et al., 2018) may be the main source of large uncertainty there. In comparison, the uniform forcing data reduced the inter-model range in ET estimates of TRENDY LSMs. Nevertheless, it is noted that the congruence across LSMs ET estimates doesn't necessarily mean they are the correct representation of ET. The narrower inter-model range may suggest shared biases. All remote sensing models and machine learning algorithms except GLEAM do not explicitly take the effects of soil moisture into account (Table S1). Given that soil moisture is pivotal to both canopy conductance and soil evaporation in arid and semi-arid regions (A et al., 2019; De Kauwe et al., 2015; Medlyn et al., 2015; Purdy et al., 2018), the lack of soil moisture information also increases the bias in ET estimation. In addition, the accuracy of remotely-sensing data itself is also an uncertainty source. The retrieval of key land surface variables, such as leaf area index and surface temperature, is influenced by vegetation architecture, solar zenith angle and satellite observational angle, particularly over heterogeneous surface (Norman and Becker, 1995).

4.1.3 Uncertainty in the ET IAV in the Southern Hemisphere

In regions south of 20ºS (including Australia, southern Africa and southern South America), the ET IAVs of remote sensing models and machine learning algorithms are smaller than that of LSMs (Fig. 4 and 5), although their spatial patterns are similar. In these regions, GLEAM, the only remote sensing model that explicitly considers the effects of soil moisture, has larger ET IAVs than other remote sensing models and has similar ET IAVs with LSMs (Fig. S4). This could imply that most existing remote sensing models may underestimate ET IAVs in the Southern Hemisphere because the effects of soil moisture are not explicitly considered. Machine learning algorithms show much smaller IAVs than other models (Fig. 4 and S4). The main reason is that ET inter-annual variability is partly neglected in the training process because the magnitude of ET inter-annual variability is usually smaller than the spatial and seasonal variability (Anav et al., 2015; Jung et al., 2019). Moreover, the IAV of satellite-based key land surface variables such as LAI, fAPAR and surface temperature may be not reliable because of the effects of clouds, which also affects the estimation of IAV of satellite-based ET. It is noted that LSMs ET IAVs show large differences in latitudes south of 20ºS (Fig. 5). This divergence in ET IAV indicates that LSMs need better representation of ET response to climate in the Southern Hemisphere.

4.1.4 Uncertainty in global ET trend

All the three categories of ET models detected an overall increasing trend in global terrestrial ET since the early 1980s, which is in agreement with previous studies (Mao et al., 2015; Miralles et al., 2014; Zeng et al., 2018a; Zeng et al., 2018b; Zeng et al., 2014; Zhang et al., 2015; Zhang et al., 2016b). Benchmark products generally suggested stronger ET intensification than LSMs. The weaker ET intensification in LSMs may be induced by the response of stomatal conductance to increasing atmospheric CO_2 concentration. The increasing CO_2 affects ET in two ways. On one

571 hand, increasing CO_2 can effectively reduce stomatal conductance and thus decrease transpiration

572 (Heijmans et al., 2001; Leipprand and Gerten, 2006; Swann et al., 2016); on the other hand, it can

573 increase vegetation productivity and thus increase LAI. For benchmarks, the second effect could

574 be captured by remotely sensed LAI, NDVI or fAPAR, while the first effect was neglected by all

575 models except P-LSH (Zhang et al., 2015). In contrast, both effects were modeled in all TRENDY

576 LSMs.

577 LAI dynamics have significant influences on ET. The increased LAI trend (greening) since the

578 early 1980s was reported by previous studies (Mao et al., 2016; Zhu et al., 2016) and is also

579 confirmed by remote sensing data and all TRENDY LSMs used in this study (Table 2 and Fig.

580 S5). Zhang et al. (2015) found that the increasing trend of global terrestrial ET over 1982-2013

581 was mainly driven by an increase in LAI and the enhanced atmosphere water demand. Using a

582 land–atmosphere coupled global climate model (GCM), Zeng et al. (2018b) further estimated that

583 global LAI increased about 8%, resulting in an increase of 0.40 ± 0.08 mm yr^{-2} in global ET

584 (contributing to $55\%\pm25\%$ of the ET increase). This number is close to the estimates of ensemble

585 LSMs (0.37 ± 0.18 mm yr^{-2}). In comparison, remote sensing models and machine learning

586 algorithms used in this study suggested smaller greening-induced ET increases. It is noted that

587 TRENDY LSMs still showed a larger discrepancy in terms of the effect of vegetation greening on

588 terrestrial ET than remote sensing physical models (Table 2) because of the significant differences

589 in LAI trend (1.74-13.63×10^{-3} m^2 m^{-2} yr^{-1}) and in the sensitivity of ET to LAI (4.04-217.39 mm

590 yr^{-2} per m^2 m^{-2}). Uncertainties in LAI trend may arise from inappropriate carbon allocations and

591 deficits in responding to water deficits (Anav et al., 2013; Hu et al., 2018; Murray-Tortarolo et al.,

592 2013; Restrepo-Coupe et al., 2017). Additionally, for machine-learning algorithms, the results

593   from insufficient long-term in situ measurements and sparse observations in tropical, boreal and

594   arid regions imply that there likely are deficiencies in representing the temporal variations.

595   **4.1.5 Lack of knowledge of the effects of irrigation**

596   Irrigation accounts for about 90% of human consumptive water use and largely affects ET in

597   irrigated croplands (Siebert et al., 2010). Global water withdrawals for irrigation were estimated

598   to be within the range of 1161-3800 km^3 yr^{-1} around the year 2000, and largely increased during

599   the period 2000-2014 (Chen et al., 2019). However, none of the remote sensing-based physical

600   models and machine-learning algorithms explicitly accounted for the effects of irrigation on ET,

601   although these effects could be taken into account to some extent by using observed LAI, NDVI,

602   or fAPAR to drive the models (Zhang et al., 2015). Considering that annual ET may surpass annual

603   precipitation in cropland, Zhang et al. (2016b) used the Budyko hydrometeorological model to

604   constrain PML-CSIRO model only in grids covered by non-crop vegetation. But the process of

605   irrigation affecting evaporation was still not taken into consideration. For TRENDY LSMs, only

606   2 of 14 models (DLEM and ISAM) included the irrigation processes (Le Quéré et al., 2018).

607   Therefore, the effects of irrigation are largely neglected in existing global ET datasets, which

608   reduces the accuracy of local ET estimates in regions with a large proportion of irrigated cropland.

609   **4.1.6 ET variability across precipitation gradient and its planetary boundary**

610   Precipitation is the source of terrestrial evapotranspiration. According to Fig. 9a, the vast majority

611   of models agree that ET has the largest IAV in regions with annual precipitation between 700 mm

612   and 1000 mm, although the magnitude of ET IAV has substantial discrepancies among different

613   models. The low ET IAV in arid and semi-arid regions doesn't mean ET is stable in these regions.

614   In fact, ET has the largest coefficient of variation (CoV, the ratio of ET standard deviation to ET

615   mean value) in arid regions, and all models show a clear negative trend of CoV with increasing

616   precipitation (Fig. 9b). This is mainly caused by the large CoV of precipitation in arid regions

617   (Fatichi et al., 2012).

618   In comparison, terrestrial ET shows a much smaller IAV at the global scale (Table 2), ranging

619   from 4.8 to 12.2 mm yr^{-1} (one standard deviation), which only equals to 1.0-1.8% of global annual

620   mean ET. The model results suggest that global terrestrial ET stabilizes at about 6.74×10^4 km^3 yr^{-}

621   ^{1} (603 mm yr^{-1}), which is close to previous estimates (Alton et al., 2009; Mueller et al., 2011; Oki

622   and Kanae, 2006; Zeng et al., 2012).The stability of global terrestrial ET is probably based on

623   partitioning the solar constant and suggests that, at a global scale, droughts in one place are

624   balanced by excess rain in other places so it all evens out. It implies that ET also has a potential

625   planetary boundary, a suggestion made by Running (2012) on NPP as a planetary boundary. ET

626   integrates four aspects of the current planetary boundaries defined by Steffen et al. (2015) : climate

627   change, freshwater use, land-system change, and biochemical flows. Given ET's importance in

628   linking terrestrial water, carbon, nutrient and energy cycles, more studies on the ET planetary

629   boundary are needed under the background of intensifying global change and increasing human

630   perturbations on the Earth system.
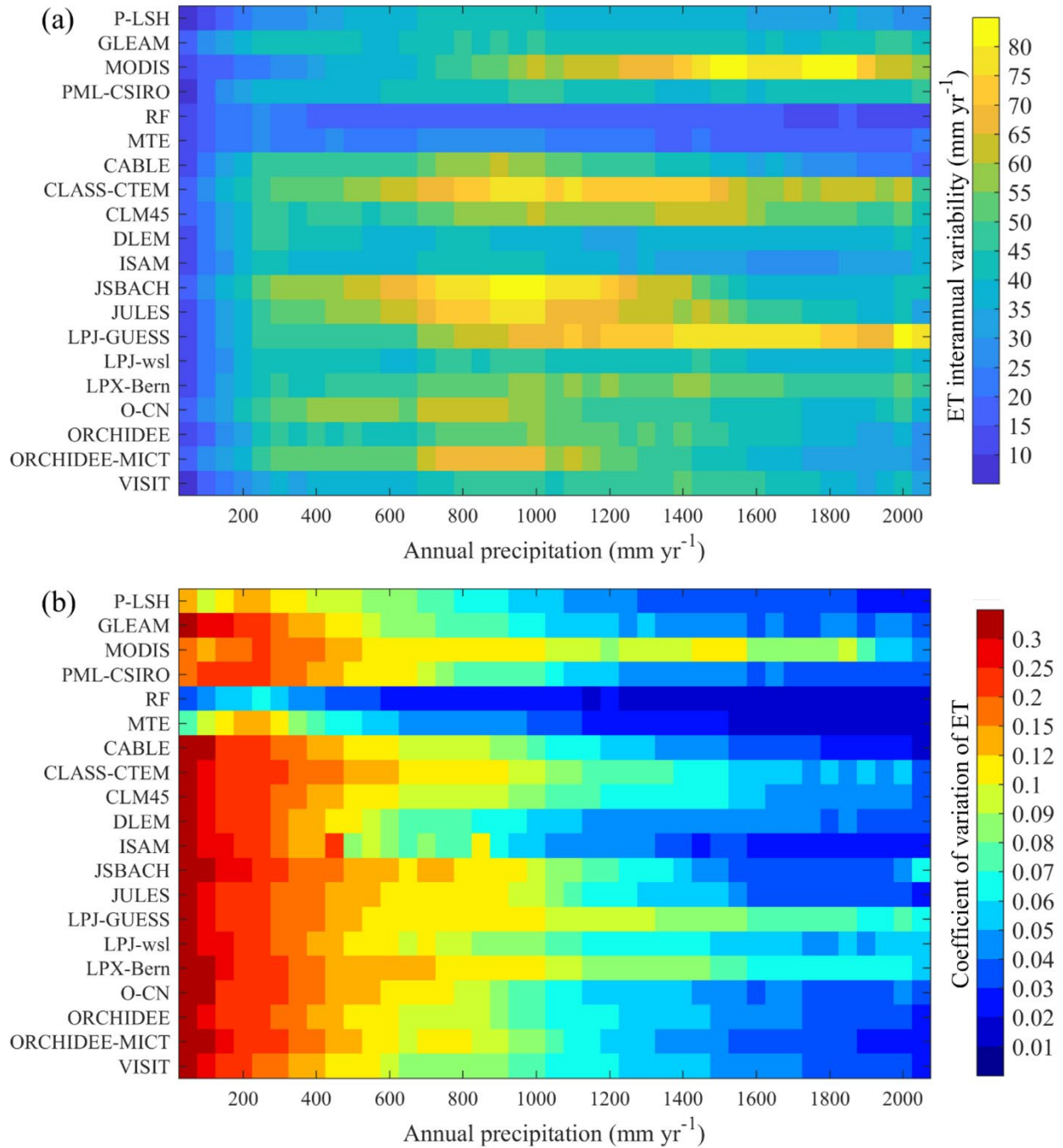
Figure 9. Interannual variability (a) and coefficient of variation (b) of ET in each 50mm interval of mean annual precipitation.

In short, the multi-model inter-comparison indicates that considerable uncertainty exists in both the temporal and spatial variations in global ET estimates, even though a large portion of models

636   adopt similar ET algorithms (Table 1). The major uncertainty source is different for different types

637   of models and regions. The uncertainty is induced by multiple factors, including problems

638   pertinent to parameterization of land processes, lack of in situ measurements, remote sensing

639   acquisition, scaling effects and meteorological forcing. Based on the results of different

640   approaches, we suggest that global terrestrial ET also has a potential planetary boundary, with the

641   value being about 6.74×10^4 km^3 yr^{-1} (603 mm yr^{-1}), which is consistent with previous estimates.

642   **4.2 Recommendations for future development**

643   **4.2.1 Remote sensing-based physical methods**

644   In the past decades, the development of remote sensing technologies has contributed to the boom

645   of various ET estimating methods. However, there is still a large room for remote sensing

646   technologies to improve (Fisher et al., 2017). Developing new platforms and sensors that have

647   improved global spatiotemporal coverage and using multi-band, multi-source remote sensing data

648   are the key points. Planned or newly launched satellites, such as NASA's GRACE Follow-On

649   (GRACE-FO) mission and ECOsystem Spaceborne Thermal Radiometer Experiment on Space

650   Station (ECOSTRESS) mission, will improve the accuracy of terrestrial ET estimates.

651   ECOSTRESS's thermal infrared (TIR) multispectral scanner is capable of monitoring diurnal

652   temperature patterns at high-resolutions, which gives insights into plant response to water stress

653   and the means to understand sub-daily ET dynamics (Hulley et al.). GRACE Follow-On

654   observations can be used to constrain subsurface lateral water transfers, which helps to correct soil

655   moisture and subsequently improves the accuracy of ET estimates (Rouholahnejad and Martens,

656   2018). Moreover, building integrated methods that fuse different ET estimates or the upstream

657   satellite-based biophysical variables from different platforms and the other forcing data will be

658 helpful to improve the accuracy and spatiotemporal coverage of ET (Ke et al., 2016; Ma et al.,

659 2018; Semmens et al., 2016).

660 The theories and retrieval algorithms of ET and related key biophysical variables also need to be

661 further improved. For example, the method for canopy conductance calculation may be improved

662 by integrating remote sensing based solar-induced chlorophyll fluorescence (SIF) data. SIF data

663 in existing Global Ozone Monitoring Experiment-2 (GOME-2), Orbiting Carbon Observatory-2

664 (OCO-2) and TROPOspheric Monitoring Instrument (TROPOMI) and the forthcoming OCO-3

665 and Geostationary Carbon Cycle Observatory (GeoCarb) satellites provide a good opportunity for

666 diagnosing transpiration and for ET partitioning at multiple spatiotemporal scales (Pagán et al.,

667 2019; Stoy et al., 2019; Sun et al., 2017). Theoretical advancements in nonequilibrium

668 thermodynamics and Maximum Entropy Production (MEP) could be incorporated into the

669 classical ET theories (Xu et al., 2019; Zhang et al., 2016a). In addition, quantifying the effects of

670 CO_2 fertilization on stomatal conductance is pivotal for remote sensing models to capture the long-

671 term trend of terrestrial ET.

672 Most existing remote sensing-based ET studies focused on total ET, however, the partitioning of

673 ET between transpiration, soil evaporation, and canopy interception may have significant

674 divergence even though the total ET is accurately estimated (Talsma et al., 2018b). In current

675 remote sensing-based ET models, soil evaporation, which is sensitive to precipitation events and

676 soil moisture, is the part with the largest error (Talsma et al., 2018a). Therefore incorporating the

677 increasing accessible satellite-based precipitation, soil moisture observations and soil property

678 data will contribute to the improvement of soil evaporation estimation. Meanwhile, the

679 consideration of soil evaporation under herbaceous vegetation and canopy will also reduce the

680 errors.

4.2.2 Machine learning methods

It is well known that the capability of machine-learning algorithms in providing accurate ET estimates largely depends on the representativeness of training datasets in describing ecosystem behaviors (Yao et al., 2017). As a result, machine-learning algorithms may not perform well outside the range of the data used for their training. Unfortunately, long-term field observations out of northern temperate regions are still insufficient. This is an important cause of the small spatial gradient and small IAVs of machine-learning ET. Given that remote sensing is capable of providing broad coverage of key biophysical variables at reasonable spatial and temporal resolutions, one way to overcome this challenge is to exclusively use remote sensing observations as training data (Jung et al., 2019; Poon and Kinoshita, 2018). Another simple way to make IAVs of machine-learning ET more realistic is normalizing the yearly anomalies when comparing with ET estimates from LSMs and remote sensing physical models (Jung et al., 2019). New machine-learning techniques, including the extreme learning machine and the adaptive neuro-fuzzy inference system, can be used to improve the accuracy of ET estimation (Gocic et al., 2016; Kişi and Tombul, 2013). The emerging deep learning methods such as recurrent neural network (RNN) and Long Short-Term Memory (LSTM) have large potential to outcompete conventional machine-learning methods in modelling ET time series (Reichstein et al., 2018; Reichstein et al., 2019). Almost all machine-learning datasets used precipitation rather soil moisture as explanatory variable when training. However, soil moisture rather than precipitation directly controls ET. As more and more global remote sensing based soil moisture datasets become available, using soil moisture products as input is expected to improve the accuracy of ET estimates, especially for regions with sparse vegetation coverage (Xu et al., 2018).

4.2.3 Land surface models

704   In contrast to observation-based methods, LSMs are able to project future changes in ET, and can

705   disentangle the effects of different drivers on ET through factorial analysis. However, results from

706   LSMs are only as good as their parameterizations of complex land surface processes which are

707   limited by our incomplete understanding of physical and biological processes (Niu et al., 2011).

708   Although TRENDY LSMs are the state-of-the-art process-based global land surfaces models,

709   improvements are still needed because several important processes are missing or not being

710   appropriately parameterized. Most of the TRENDY LSMs did not simulate the processes relevant

711   to human management including irrigation (Chen et al., 2019) and application of fertilizers (Mao

712   et al., 2015), and natural disturbances like wildfire (Poon and Kinoshita, 2018). Incorporating these

713   processes into present LSMs is critical, although introduction of new model parameters potentially

714   also leads to an increase in a model's uncertainty.

715   In light of the importance of soil water availability in constraining canopy conductance and

716   dynamics, accurate representation of hydrological processes is a core task for LSMs, particularly

717   in dry regions. Integrating a dynamic root water uptake function and hydraulic redistribution into

718   the LSM can significantly improve its performance of estimating seasonal ET and soil moisture

719   (Li et al., 2012). Moreover, other hydrological processes including groundwater (Decker, 2015),

720   lateral flow (Rouholahnejad and Martens, 2018) and water vapor diffusion at the soil surface

721   (Chang et al., 2018) need to be simulated and correctly represented to reproduce the dynamics of

722   soil water and ET. Since canopy LAI plays an important role in regulating ET, correctly simulating

723   vegetation dynamics is also critical. One way is to correct the initialization, distribution, and

724   parameterization of vegetation phenology in LSMs (Murray-Tortarolo et al., 2013; Zhang et al.,

725   2019). Appropriate carbon allocation scheme and parameterization of vegetation's response to

726   water deficits are also important for reproducing vegetation dynamics (Anav et al., 2013).

5. Conclusion

In this study, we evaluated twenty global terrestrial ET estimates including four from remote sensing-based physical models, two from machine-learning algorithms and fourteen from TRENDY LSMs. The ensemble mean values of global terrestrial ET for the three categories agreed well, ranging from 589.6 mm yr^{-1} to 617.1 mm yr^{-1}. All the three categories detected an overall increasing trend in global ET during the period 1982-2011 and suggested a positive effect of vegetation greening on ET intensification. However, the multi-model inter-comparison indicates that considerable uncertainties still exist in both temporal and spatial variations in global terrestrial ET estimates. LSMs had significant differences in the ET magnitude in tropical regions, especially the Amazon Basin, while benchmark ET products showed larger inter-model range in arid and semi-arid regions than LSMs. Trends in ET estimates also showed significant discrepancies among LSMs. These uncertainties are induced by parameterization of land processes, meteorological forcings, lack of in-situ measurements, remote sensing acquisition and scaling effects. Model developments and observational improvements provide two parallel pathways towards improving the accuracy of global terrestrial ET estimation.

Code and data availability

TRENDYv6 data are available from S.S. (s.a.sitch@exeter.ac.uk) on reasonable request. MODIS ET data are available from http://files.ntsg.umt.edu/data/NTSG_Products/MOD16/. GLEAM ET are available from https://www.gleam.eu/. Both Model Tree Ensemble and Random Forest ET are available from https://www.bgc-jena.mpg.de/geodb/projects/FileDetails.php. P-LSH ET are available from http://files.ntsg.umt.edu/data/ET_global_monthly/Global_8kmResolution/. PML-CSIRO ET are from https://data.csiro.au/dap/landingpage?pid=csiro:17375. CRU-

749 NCEPv8 data are available from Nicolas Viovy on reasonable request. GIMMS LAI3gV1 data are

750 available from R. B. Myneni on reasonable request. GIMMS NDVI3gV1 data are available from

751 https://ecocast.arc.nasa.gov/data/pub/gimms/3g.v1/.

Author contributions

753 S.P. initiated this research and was responsible for the integrity of the work as a whole. N.P. carried

754 out the analyses. S.P., N.P., H.T. and H.S. wrote the manuscript with contributions from all

755 authors. P.F., S.S., V.K.A., V.H., A.K.J., E.K., S.L., D.L., J.E.M.S.N., C.O., B.P., H.T. and S.Z.

756 contributed to the TRENDY results.

Competing interests

758 The authors declare that they have no conflict of interest.

Acknowledgements

760 This study has been supported partially by grants from National Science Foundation (1903722 and

761 1243232), AU-OUC Joint Center Program and Auburn University IGP Program. A.K.J. was

762 support in part by Department of Energy (No. DE‑SC0016323) and NSF (NSF AGS 12-43071).

763 D.L. acknowledges funding from the National Institute of Food and Agriculture/US Department

764 of Agriculture (2015- 67003-23489 and 2015-67003-23485). S.L. acknowledges support from EC

765 H2020 (CCiCC; grant no 821003) and SNSF (grant no. 20020_172476). V.H. acknowledges

766 support from the Earth Systems and Climate Change Hub, funded by the Australian Government's

767 National Environmental Science Program. We thank all people who provided data used in this

768 study, in particular, the TRENDY modelling groups. Additional details on funding support for the

769 participating 14 land surface models have been provided in the TRENDY Project.

770

References

771 A, Y., Wang, G., Liu, T., Xue, B., and Kuczera, G.: Spatial variation of correlations between
772 vertical soil water and evapotranspiration and their controlling factors in a semi-arid region,
773 Journal of Hydrology, 574, 53-63, 2019.
774 Abramopoulos, F., Rosenzweig, C., and Choudhury, B.: Improved ground hydrology calculations
775 for global climate models (GCMs): Soil water movement and evapotranspiration, Journal of
776 Climate, 1, 921-941, 1988.
777 Allen, R. G., Pereira, L. S., Raes, D., and Smith, M.: Crop evapotranspiration-Guidelines for
778 computing crop water requirements-FAO Irrigation and drainage paper 56, Fao, Rome, 300,
779 D05109, 1998.
780 Alton, P., Fisher, R., Los, S., and Williams, M.: Simulations of global evapotranspiration using
781 semiempirical and mechanistic schemes of plant hydrology, Global biogeochemical cycles, 23,
782 2009.
783 Anav, A., Friedlingstein, P., Beer, C., Ciais, P., Harper, A., Jones, C., Murray‐Tortarolo, G., Papale,
784 D., Parazoo, N. C., and Peylin, P.: Spatiotemporal patterns of terrestrial gross primary
785 production: A review, Reviews of Geophysics, 53, 785-818, 2015.
786 Anav, A., Murray-Tortarolo, G., Friedlingstein, P., Sitch, S., Piao, S., and Zhu, Z.: Evaluation of
787 land surface models in reproducing satellite Derived leaf area index over the high-latitude
788 northern hemisphere. Part II: Earth system models, Remote Sensing, 5, 3637-3661, 2013.
789 Antonopoulos, V. Z., Gianniou, S. K., and Antonopoulos, A. V.: Artificial neural networks and
790 empirical equations to estimate daily evaporation: application to lake Vegoritis, Greece,
791 Hydrological Sciences Journal, 61, 2590-2599, 2016.
792 Barman, R., Jain, A. K., and Liang, M.: Climate‐driven uncertainties in modeling terrestrial
793 energy and water fluxes: a site‐level to global‐scale analysis, Global change biology, 20, 1885-
794 1900, 2014.
795 Bodesheim, P., Jung, M., Gans, F., Mahecha, M. D., and Reichstein, M.: Upscaled diurnal cycles
796 of land–atmosphere fluxes: a new global half-hourly data product, Earth Syst. Sci. Data, 10,
797 1327-1365, 2018.
798 Breiman, L.: Random forests, Machine learning, 45, 5-32, 2001.
799 Chang, L.-L., Dwivedi, R., Knowles, J. F., Fang, Y.-H., Niu, G.-Y., Pelletier, J. D., Rasmussen, C.,
800 Durcik, M., Barron-Gafford, G. A., and Meixner, T.: Why Do Large-Scale Land Surface Models
801 Produce a Low Ratio of Transpiration to Evapotranspiration?, Journal of Geophysical Research:
802 Atmospheres, 123, 9109-9130, 2018.
803 Chen, Y., Feng, X., Fu, B., Shi, W., Yin, L., and Lv, Y.: Recent global cropland water consumption
804 constrained by observations, Water Resources Research, 2019. 2019.
805 Chen, Y., Xia, J., Liang, S., Feng, J., Fisher, J. B., Li, X., Li, X., Liu, S., Ma, Z., and Miyata, A.:
806 Comparison of satellite-based evapotranspiration models over terrestrial ecosystems in China,
807 Remote Sensing of Environment, 140, 279-293, 2014.
808 Clark, M. P., Fan, Y., Lawrence, D. M., Adam, J. C., Bolster, D., Gochis, D. J., Hooper, R. P., Kumar,
809 M., Leung, L. R., and Mackay, D. S.: Improving the representation of hydrologic processes in
810 Earth System Models, Water Resources Research, 51, 5929-5956, 2015.

812 Cleugh, H. A., Leuning, R., Mu, Q., and Running, S. W.: Regional evaporation estimates from flux
813 tower and MODIS satellite data, Remote Sensing of Environment, 106, 285-304, 2007.
814 d'Orgeval, T., Polcher, J., and Rosnay, P. d.: Sensitivity of the West African hydrological cycle in
815 ORCHIDEE to infiltration processes, Hydrology and Earth System Sciences, 12, 1387-1401, 2008.
816 Dai, A.: Precipitation characteristics in eighteen coupled climate models, Journal of Climate, 19,
817 4605-4630, 2006.
818 De Kauwe, M. G., Kala, J., Lin, Y.-S., Pitman, A. J., Medlyn, B. E., Duursma, R. A., Abramowitz, G.,
819 Wang, Y., and Gonzalez Miralles, D.: A test of an optimal stomatal conductance scheme within
820 the CABLE land surface model, Geoscientific Model Development, 8, 431-452, 2015.
821 Decker, M.: Development and evaluation of a new soil moisture and runoff parameterization
822 for the CABLE LSM including subgrid-scale processes, Journal of Advances in Modeling Earth
823 Systems, 7, 1788-1809, 2015.
824 Dou, X. and Yang, Y.: Evapotranspiration estimation using four different machine learning
825 approaches in different terrestrial ecosystems, Computers and Electronics in Agriculture, 148,
826 95-106, 2018.
827 Douville, H., Ribes, A., Decharme, B., Alkama, R., and Sheffield, J.: Anthropogenic influence on
828 multidecadal changes in reconstructed global evapotranspiration, Nature Climate Change, 3,
829 59, 2013.
830 Famiglietti, J. and Wood, E. F.: Evapotranspiration and runoff from large land areas: Land
831 surface hydrology for atmospheric general circulation models, Surveys in Geophysics, 12, 179-
832 204, 1991.
833 Fatichi, S., Ivanov, V. Y., and Caporali, E.: Investigating Interannual Variability of Precipitation at
834 the Global Scale: Is There a Connection with Seasonality?, Journal of Climate, 25, 5512-5523,
835 2012.
836 Feng, Y., Cui, N., Gong, D., Zhang, Q., and Zhao, L.: Evaluation of random forests and generalized
837 regression neural networks for daily reference evapotranspiration modelling, Agricultural
838 Water Management, 193, 163-173, 2017.
839 Fisher, J. B., Malhi, Y., Bonal, D., Da Rocha, H. R., De Araujo, A. C., Gamo, M., Goulden, M. L.,
840 Hirano, T., Huete, A. R., and Kondo, H.: The land–atmosphere water flux in the tropics, Global
841 Change Biology, 15, 2694-2714, 2009.
842 Fisher, J. B., Melton, F., Middleton, E., Hain, C., Anderson, M., Allen, R., McCabe, M. F., Hook, S.,
843 Baldocchi, D., and Townsend, P. A.: The future of evapotranspiration: Global requirements for
844 ecosystem functioning, carbon and climate feedbacks, agricultural management, and water
845 resources, Water Resources Research, 53, 2618-2626, 2017.
846 Fisher, J. B., Tu, K. P., and Baldocchi, D. D.: Global estimates of the land–atmosphere water flux
847 based on monthly AVHRR and ISLSCP-II data, validated at 16 FLUXNET sites, Remote Sensing of
848 Environment, 112, 901-919, 2008.
849 Fu, B. P.: On the calculation of the evaporation from land surface, Sci. Atmos. Sin, 5, 23-31,
850 1981.
851 Fu, G., Charles, S. P., and Yu, J.: A critical overview of pan evaporation trends over the last 50
852 years, Climatic change, 97, 193, 2009.
853 Gedney, N., Cox, P., Betts, R., Boucher, O., Huntingford, C., and Stott, P.: Detection of a direct
854 carbon dioxide effect in continental river runoff records, Nature, 439, 835, 2006.

855 Glenn, E. P., Nagler, P. L., and Huete, A. R.: Vegetation index methods for estimating
856 evapotranspiration by remote sensing, Surveys in Geophysics, 31, 531-555, 2010.
857 Gocic, M., Petković, D., Shamshirband, S., and Kamsin, A.: Comparative analysis of reference
858 evapotranspiration equations modelling by extreme learning machine, Computers and
859 Electronics in Agriculture, 127, 56-63, 2016.
860 Good, S. P., Noone, D., and Bowen, G.: Hydrologic connectivity constrains partitioning of global
861 terrestrial water fluxes, Science, 349, 175-177, 2015.
862 Guimberteau, M., Zhu, D., Maignan, F., Huang, Y., Chao, Y., Dantec-Nédélec, S., Ottlé, C., Jornet-
863 Puig, A., Bastos, A., and Laurent, P.: ORCHIDEE-MICT (v8. 4.1), a land surface model for the high
864 latitudes: model description and validation, Geoscientific Model Development, 11, 121, 2018.
865 Haverd, V., Smith, B., Nieradzik, L., Briggs, P. R., Woodgate, W., Trudinger, C. M., Canadell, J. G.,
866 and Cuntz, M.: A new version of the CABLE land surface model (Subversion revision r4601)
867 incorporating land use and land cover change, woody vegetation demography, and a novel
868 optimisation-based approach to plant coordination of photosynthesis, Geosci. Model Dev., 11,
869 2995-3026, 2018.
870 Heijmans, M. M., Arp, W. J., and Berendse, F.: Effects of elevated CO2 and vascular plants on
871 evapotranspiration in bog vegetation, Global Change Biology, 7, 817-827, 2001.
872 Hu, Z., Shi, H., Cheng, K., Wang, Y. P., Piao, S., Li, Y., Zhang, L., Xia, J., Zhou, L., and Yuan, W.:
873 Joint structural and physiological control on the interannual variation in productivity in a
874 temperate grassland: A data–model comparison, Global change biology, 24, 2965-2979, 2018.
875 Huang, S., Bartlett, P., and Arain, M. A.: Assessing nitrogen controls on carbon, water and
876 energy exchanges in major plant functional types across North America using a carbon and
877 nitrogen coupled ecosystem model, Ecological modelling, 323, 12-27, 2016.
878 Hulley, G., Hook, S., Fisher, J., and Lee, C.: ECOSTRESS, A NASA Earth-Ventures Instrument for
879 studying links between the water cycle and plant health over the diurnal cycle, 2017 IEEE
880 International Geoscience and Remote Sensing Symposium (IGARSS), 2017, 5494-5496.
881 Ito, A.: Evaluation of the impacts of defoliation by tropical cyclones on a Japanese forest's
882 carbon budget using flux data and a process–based model, Journal of Geophysical Research:
883 Biogeosciences, 115, 2010.
884 Jackson, R., Reginato, R., and Idso, S.: Wheat canopy temperature: a practical tool for
885 evaluating water requirements, Water resources research, 13, 651-656, 1977.
886 Jimenez, C., Prigent, C., Mueller, B., Seneviratne, S. I., McCabe, M., Wood, E., Rossow, W.,
887 Balsamo, G., Betts, A., and Dirmeyer, P.: Global intercomparison of 12 land surface heat flux
888 estimates, Journal of Geophysical Research: Atmospheres, 116, 2011.
889 Jung, M., Koirala, S., Weber, U., Ichii, K., Gans, F., Camps-Valls, G., Papale, D., Schwalm, C.,
890 Tramontana, G., and Reichstein, M.: The FLUXCOM ensemble of global land-atmosphere energy
891 fluxes, Scientific Data, 6, 74, 2019.
892 Jung, M., Reichstein, M., and Bondeau, A.: Towards global empirical upscaling of FLUXNET eddy
893 covariance observations: validation of a model tree ensemble approach using a biosphere
894 model, Biogeosciences, 6, 2001-2013, 2009.
895 Jung, M., Reichstein, M., Ciais, P., Seneviratne, S. I., Sheffield, J., Goulden, M. L., Bonan, G.,
896 Cescatti, A., Chen, J., and De Jeu, R.: Recent decline in the global land evapotranspiration trend
897 due to limited moisture supply, Nature, 467, 951, 2010.

898   Jung, M., Reichstein, M., Margolis, H. A., Cescatti, A., Richardson, A. D., Arain, M. A., Arneth, A.,
899   Bernhofer, C., Bonal, D., and Chen, J.: Global patterns of land–atmosphere fluxes of carbon
900   dioxide, latent heat, and sensible heat derived from eddy covariance, satellite, and
901   meteorological observations, Journal of Geophysical Research: Biogeosciences, 116, 2011.
902   Jung, M., Reichstein, M., Schwalm, C. R., Huntingford, C., Sitch, S., Ahlström, A., Arneth, A.,
903   Camps-Valls, G., Ciais, P., and Friedlingstein, P.: Compensatory water effects link yearly global
904   land CO_2 sink changes to temperature, Nature, 541, 516-520, 2017.
905   Ke, Y., Im, J., Park, S., and Gong, H.: Downscaling of MODIS One kilometer evapotranspiration
906   using Landsat-8 data and machine learning approaches, Remote Sensing, 8, 215, 2016.
907   Keller, K. M., Lienert, S., Bozbiyik, A., Stocker, T. F., Frank, D. C., Klesse, S., Koven, C. D.,
908   Leuenberger, M., Riley, W. J., and Saurer, M.: 20th century changes in carbon isotopes and
909   water-use efficiency: tree-ring-based evaluation of the CLM4. 5 and LPX-Bern models,
910   Biogeosciences (Online), 14, 2017.
911   Kendall, M. G.: Rank correlation methods, 1955. 1955.
912   Khan, M. S., Liaqat, U. W., Baik, J., and Choi, M.: Stand-alone uncertainty characterization of
913   GLEAM, GLDAS and MOD16 evapotranspiration products using an extended triple collocation
914   approach, Agricultural and Forest Meteorology, 252, 256-268, 2018.
915   Kisi, O., Sanikhani, H., Zounemat-Kermani, M., and Niazi, F.: Long-term monthly
916   evapotranspiration modeling by several data-driven methods without climatic data, Computers
917   and Electronics in Agriculture, 115, 66-77, 2015.
918   Kişi, Ö. and Tombul, M.: Modeling monthly pan evaporations using fuzzy genetic approach,
919   Journal of hydrology, 477, 203-212, 2013.
920   Knauer, J., Werner, C., and Zaehle, S.: Evaluating stomatal models and their atmospheric
921   drought response in a land surface scheme: A multibiome analysis, Journal of Geophysical
922   Research: Biogeosciences, 120, 1894-1911, 2015.
923   Lawrence, D. M., Thornton, P. E., Oleson, K. W., and Bonan, G. B.: The partitioning of
924   evapotranspiration into transpiration, soil evaporation, and canopy evaporation in a GCM:
925   Impacts on land–atmosphere interaction, Journal of Hydrometeorology, 8, 862-880, 2007.
926   Le Quéré, C., Andrew, R. M., Friedlingstein, P., Sitch, S., Pongratz, J., Manning, A. C.,
927   Korsbakken, J. I., Peters, G. P., Canadell, J. G., and Jackson, R. B.: Global carbon budget 2017,
928   Earth Syst. Sci. Data, 10, 405-448, 2018.
929   Leipprand, A. and Gerten, D.: Global effects of doubled atmospheric CO_2 content on
930   evapotranspiration, soil moisture and runoff under potential natural vegetation, Hydrological
931   Sciences Journal, 51, 171-185, 2006.
932   Leuning, R., Zhang, Y., Rajaud, A., Cleugh, H., and Tu, K.: A simple surface conductance model to
933   estimate regional evaporation using MODIS leaf area index and the Penman–Monteith
934   equation, Water Resources Research, 44, 2008.
935   Li, J., Wang, Y. P., Duan, Q., Lu, X., Pak, B., Wiltshire, A., Robertson, E., and Ziehn, T.:
936   Quantification and attribution of errors in the simulated annual gross primary production and
937   latent heat fluxes by two global land surface models, Journal of Advances in Modeling Earth
938   Systems, 8, 1270-1288, 2016.
939   Li, L., Wang, Y. P., Yu, Q., Pak, B., Eamus, D., Yan, J., Gorsel, E., and Baker, I. T.: Improving the
940   responses of the Australian community land surface model (CABLE) to seasonal drought,
941   Journal of Geophysical Research: Biogeosciences, 117, 2012.

942 Li, Z.-L., Tang, R., Wan, Z., Bi, Y., Zhou, C., Tang, B., Yan, G., and Zhang, X.: A review of current
943 methodologies for regional evapotranspiration estimation from remotely sensed data, Sensors,
944 9, 3801-3853, 2009.
945 Lian, X., Piao, S., Huntingford, C., Li, Y., Zeng, Z., Wang, X., Ciais, P., McVicar, T. R., Peng, S., and
946 Ottlé, C.: Partitioning global land evapotranspiration using CMIP5 models constrained by
947 observations, Nature Climate Change, 8, 640, 2018.
948 Liu, M., Tian, H., Chen, G., Ren, W., Zhang, C., and Liu, J.: Effects of Land‑Use and Land‑Cover
949 Change on Evapotranspiration and Water Yield in China During 1900‑2000 1, JAWRA Journal of
950 the American Water Resources Association, 44, 1193-1207, 2008.
951 Ma, Y., Liu, S., Song, L., Xu, Z., Liu, Y., Xu, T., and Zhu, Z.: Estimation of daily evapotranspiration
952 and irrigation water efficiency at a Landsat-like scale for an arid irrigation area using multi-
953 source remote sensing data, Remote Sensing of Environment, 216, 715-734, 2018.
954 Mann, H. B.: Nonparametric tests against trend, Econometrica: Journal of the Econometric
955 Society, 1945. 245-259, 1945.
956 Mao, J., Fu, W., Shi, X., Ricciuto, D. M., Fisher, J. B., Dickinson, R. E., Wei, Y., Shem, W., Piao, S.,
957 and Wang, K.: Disentangling climatic and anthropogenic controls on global terrestrial
958 evapotranspiration trends, Environmental Research Letters, 10, 094008, 2015.
959 Mao, J., Ribes, A., Yan, B., Shi, X., Thornton, P. E., Séférian, R., Ciais, P., Myneni, R. B., Douville,
960 H., and Piao, S.: Human-induced greening of the northern extratropical land surface, Nature
961 Climate Change, 2016. 2016.
962 Martens, B., Gonzalez Miralles, D., Lievens, H., van der Schalie, R., de Jeu, R. A., Fernández-
963 Prieto, D., Beck, H. E., Dorigo, W., and Verhoest, N.: GLEAM v3: Satellite-based land evaporation
964 and root-zone soil moisture, Geoscientific Model Development, 10, 1903-1925, 2017.
965 Maselli, F., Papale, D., Chiesi, M., Matteucci, G., Angeli, L., Raschi, A., and Seufert, G.:
966 Operational monitoring of daily evapotranspiration by the combination of MODIS NDVI and
967 ground meteorological data: Application and evaluation in Central Italy, Remote sensing of
968 environment, 152, 279-290, 2014.
969 Medlyn, B. E., Zaehle, S., De Kauwe, M. G., Walker, A. P., Dietze, M. C., Hanson, P. J., Hickler, T.,
970 Jain, A. K., Luo, Y., and Parton, W.: Using ecosystem experiments to improve vegetation models,
971 Nature Climate Change, 5, 528, 2015.
972 Miralles, D., Holmes, T., De Jeu, R., Gash, J., Meesters, A., and Dolman, A.: Global land-surface
973 evaporation estimated from satellite-based observations, Hydrology and Earth System Sciences,
974 15, 453-469, 2011.
975 Miralles, D., Jiménez, C., Jung, M., Michel, D., Ershadi, A., McCabe, M., Hirschi, M., Martens, B.,
976 Dolman, A., and Fisher, J.: The WACMOS-ET project-Part 2: Evaluation of global terrestrial
977 evaporation data sets, Hydrology and Earth System Sciences, 20, 823-842, 2016.
978 Miralles, D., van den Berg, M., Gash, J., Parinussa, R., Jeu, R., Beck, H., Holmes, T., Jimenez, C.,
979 Verhoest, N., and Dorigo, W.: El Nino-La Nina cycle and recent trends in continental
980 evaporation, Nature Climate Change, 4, 122-126, 2014.
981 Monteith, J. L.: Evaporation and environment, 1965, 4.
982 Mu, Q., Heinsch, F. A., Zhao, M., and Running, S. W.: Development of a global
983 evapotranspiration algorithm based on MODIS and global meteorology data, Remote sensing of
984 Environment, 111, 519-536, 2007.

985 Mu, Q., Zhao, M., and Running, S. W.: Improvements to a MODIS global terrestrial
986 evapotranspiration algorithm, Remote Sensing of Environment, 115, 1781-1800, 2011.
987 Mueller, B., Hirschi, M., Jimenez, C., Ciais, P., Dirmeyer, P., Dolman, A., Fisher, J., Jung, M.,
988 Ludwig, F., and Maignan, F.: Benchmark products for land evapotranspiration: LandFlux-EVAL
989 multi-data set synthesis, Hydrology and Earth System Sciences, 2013. 2013.
990 Mueller, B., Seneviratne, S. I., Jimenez, C., Corti, T., Hirschi, M., Balsamo, G., Ciais, P., Dirmeyer,
991 P., Fisher, J., and Guo, Z.: Evaluation of global observations–based evapotranspiration datasets
992 and IPCC AR4 simulations, Geophysical Research Letters, 38, 2011.
993 Murray-Tortarolo, G., Anav, A., Friedlingstein, P., Sitch, S., Piao, S., Zhu, Z., Poulter, B., Zaehle,
994 S., Ahlström, A., and Lomas, M.: Evaluation of land surface models in reproducing satellite-
995 derived LAI over the high-latitude northern hemisphere. Part I: Uncoupled DGVMs, Remote
996 Sensing, 5, 4819-4838, 2013.
997 Nagler, P. L., Scott, R. L., Westenburg, C., Cleverly, J. R., Glenn, E. P., and Huete, A. R.:
998 Evapotranspiration on western US rivers estimated using the Enhanced Vegetation Index from
999 MODIS and data from eddy covariance and Bowen ratio flux towers, Remote sensing of
1000 environment, 97, 337-351, 2005.
1001 Nepstad, D., Lefebvre, P., Lopes da Silva, U., Tomasella, J., Schlesinger, P., Solórzano, L.,
1002 Moutinho, P., Ray, D., and Guerreira Benito, J.: Amazon drought and its implications for forest
1003 flammability and tree growth: A basin–wide analysis, Global change biology, 10, 704-717, 2004.
1004 Niu, G. Y., Yang, Z. L., Mitchell, K. E., Chen, F., Ek, M. B., Barlage, M., Kumar, A., Manning, K.,
1005 Niyogi, D., and Rosero, E.: The community Noah land surface model with multiparameterization
1006 options (Noah-MP): 1. Model description and evaluation with local–scale measurements,
1007 Journal of Geophysical Research: Atmospheres, 116, 2011.
1008 Noilhan, J. and Mahfouf, J.-F.: The ISBA land surface parameterisation scheme, Global and
1009 planetary Change, 13, 145-159, 1996.
1010 Norman, J. M. and Becker, F.: Terminology in thermal infrared remote sensing of natural
1011 surfaces, Remote Sensing Reviews, 12, 159-173, 1995.
1012 Oki, T. and Kanae, S.: Global hydrological cycles and world water resources, science, 313, 1068-
1013 1072, 2006.
1014 Oleson, K. W., Lawrence, D. M., Gordon, B., Flanner, M. G., Kluzek, E., Peter, J., Levis, S.,
1015 Swenson, S. C., Thornton, E., and Feddema, J.: Technical description of version 4.0 of the
1016 Community Land Model (CLM), 2010. 2010.
1017 Pagán, R. B., Maes, H. W., Gentine, P., Martens, B., and Miralles, G. D.: Exploring the Potential
1018 of Satellite Solar-Induced Fluorescence to Constrain Global Transpiration Estimates, Remote
1019 Sensing, 11, 2019.
1020 Pan, N., Feng, X., Fu, B., Wang, S., Ji, F., and Pan, S.: Increasing global vegetation browning
1021 hidden in overall vegetation greening: Insights from time-varying trends, Remote Sensing of
1022 Environment, 214, 59-72, 2018a.
1023 Pan, S., Chen, G., Ren, W., Dangal, S. R. S., Banger, K., Yang, J., Tao, B., and Tian, H.: Responses
1024 of global terrestrial water use efficiency to climate change and rising atmospheric CO_2
1025 concentration in the twenty-first century, International Journal of Digital Earth, 11, 558-582,
1026 2018b.

Pan, S., Tian, H., Dangal, S. R., Yang, Q., Yang, J., Lu, C., Tao, B., Ren, W., and Ouyang, Z.: Responses of global terrestrial evapotranspiration to climate change and increasing atmospheric CO2 in the 21st century, Earth's Future, 3, 15-35, 2015.

Peng, S., Piao, S., Ciais, P., Myneni, R. B., Chen, A., Chevallier, F., Dolman, A. J., Janssens, I. A., Penuelas, J., and Zhang, G.: Asymmetric effects of daytime and night-time warming on Northern Hemisphere vegetation, Nature, 501, 88, 2013.

Peterson, T. C., Golubev, V. S., and Groisman, P. Y.: Evaporation losing its strength, Nature, 377, 687-688, 1995.

Piao, S., Ciais, P., Huang, Y., Shen, Z., Peng, S., Li, J., Zhou, L., Liu, H., Ma, Y., and Ding, Y.: The impacts of climate change on water resources and agriculture in China, Nature, 467, 43-51, 2010.

Poon, P. and Kinoshita, A.: Estimating Evapotranspiration in a Post-Fire Environment Using Remote Sensing and Machine Learning, Remote Sensing, 10, 1728, 2018.

Priestley, C. and Taylor, R.: On the assessment of surface heat flux and evaporation using large-scale parameters, Monthly weather review, 100, 81-92, 1972.

Purdy, A. J., Fisher, J. B., Goulden, M. L., Colliander, A., Halverson, G., Tu, K., and Famiglietti, J. S.: SMAP soil moisture improves global evapotranspiration, Remote Sensing of Environment, 219, 1-14, 2018.

Reichstein, M., Besnard, S., Carvalhais, N., Gans, F., Jung, M., Kraft, B., and Mahecha, M.: Modelling Landsurface Time-Series with Recurrent Neural Nets, IGARSS 2018-2018 IEEE International Geoscience and Remote Sensing Symposium2018, 7640-7643.

Reichstein, M., Camps-Valls, G., Stevens, B., Jung, M., Denzler, J., Carvalhais, N., and Prabhat: Deep learning and process understanding for data-driven Earth system science, Nature, 566, 195-204, 2019.

Restrepo‐Coupe, N., Levine, N. M., Christoffersen, B. O., Albert, L. P., Wu, J., Costa, M. H., Galbraith, D., Imbuzeiro, H., Martins, G., and da Araujo, A. C.: Do dynamic global vegetation models capture the seasonality of carbon fluxes in the Amazon basin? A data‐model intercomparison, Global change biology, 23, 191-208, 2017.

Roderick, M. L. and Farquhar, G. D.: The cause of decreased pan evaporation over the past 50 years, science, 298, 1410-1411, 2002.

Rouholahnejad, E. and Martens, B.: Improving global estimates of terrestrial evaporation by integrating remotely-sensed observations of changes in terrestrial water storage (GRACE) into a global evaporation model (GLEAM), 2018 2018.

Running, S. W.: A measurable planetary boundary for the biosphere, science, 337, 1458-1459, 2012.

Sayemuzzaman, M. and Jha, M. K.: Seasonal and annual precipitation time series trend analysis in North Carolina, United States, Atmospheric Research, 137, 183-194, 2014.

Semmens, K. A., Anderson, M. C., Kustas, W. P., Gao, F., Alfieri, J. G., McKee, L., Prueger, J. H., Hain, C. R., Cammalleri, C., Yang, Y., Xia, T., Sanchez, L., Mar Alsina, M., and Vélez, M.: Monitoring daily evapotranspiration over two California vineyards using Landsat 8 in a multi-sensor data fusion approach, Remote Sensing of Environment, 185, 155-170, 2016.

Sen, P. K.: Estimates of the regression coefficient based on Kendall's tau, Journal of the American statistical association, 63, 1379-1389, 1968.

1070 Shrestha, N. and Shukla, S.: Support vector machine based modeling of evapotranspiration
1071 using hydro-climatic variables in a sub-tropical environment, Agricultural and forest
1072 meteorology, 200, 172-184, 2015.
1073 Siebert, S., Burke, J., Faures, J.-M., Frenken, K., Hoogeveen, J., Döll, P., and Portmann, F. T.:
1074 Groundwater use for irrigation–a global inventory, Hydrology and earth system sciences, 14,
1075 1863-1880, 2010.
1076 Simmons, A., Willett, K., Jones, P., Thorne, P., and Dee, D.: Low‐frequency variations in surface
1077 atmospheric humidity, temperature, and precipitation: Inferences from reanalyses and monthly
1078 gridded observational data sets, Journal of Geophysical Research: Atmospheres, 115, 2010.
1079 Sitch, S., Smith, B., Prentice, I. C., Arneth, A., Bondeau, A., Cramer, W., Kaplan, J., Levis, S.,
1080 Lucht, W., and Sykes, M. T.: Evaluation of ecosystem dynamics, plant geography and terrestrial
1081 carbon cycling in the LPJ dynamic global vegetation model, Global Change Biology, 9, 161-185,
1082 2003.
1083 Smith, B.: LPJ-GUESS-an ecosystem modelling framework, Department of Physical Geography
1084 and Ecosystems Analysis. INES, Sölvegatan, 12, 22362, 2001.
1085 Steffen, W., Richardson, K., Rockström, J., Cornell, S. E., Fetzer, I., Bennett, E. M., Biggs, R.,
1086 Carpenter, S. R., de Vries, W., de Wit, C. A., Folke, C., Gerten, D., Heinke, J., Mace, G. M.,
1087 Persson, L. M., Ramanathan, V., Reyers, B., and Sörlin, S.: Planetary boundaries: Guiding human
1088 development on a changing planet, Science, 347, 1259855, 2015.
1089 Stoy, P. C., El-Madany, T., Fisher, J. B., Gentine, P., Gerken, T., Good, S. P., Liu, S., Miralles, D. G.,
1090 Perez-Priego, O., Skaggs, T. H., Wohlfahrt, G., Anderson, R. G., Jung, M., Maes, W. H.,
1091 Mammarella, I., Mauder, M., Migliavacca, M., Nelson, J. A., Poyatos, R., Reichstein, M., Scott, R.
1092 L., and Wolf, S.: Reviews and syntheses: Turning the challenges of partitioning ecosystem
1093 evaporation and transpiration into opportunities, Biogeosciences Discuss., 2019, 1-47, 2019.
1094 Sun, Q., Miao, C., Duan, Q., Ashouri, H., Sorooshian, S., and Hsu, K. L.: A review of global
1095 precipitation data sets: Data sources, estimation, and intercomparisons, Reviews of Geophysics,
1096 56, 79-107, 2018.
1097 Sun, Y., Frankenberg, C., Wood, J. D., Schimel, D. S., Jung, M., Guanter, L., Drewry, D. T., Verma,
1098 M., Porcar-Castell, A., Griffis, T. J., Gu, L., Magney, T. S., Köhler, P., Evans, B., and Yuen, K.: OCO-
1099 2 advances photosynthesis observation from space via solar-induced chlorophyll fluorescence,
1100 Science, 358, eaam5747, 2017.
1101 Swann, A. L., Hoffman, F. M., Koven, C. D., and Randerson, J. T.: Plant responses to increasing
1102 CO_2 reduce estimates of climate impacts on drought severity, Proceedings of the National
1103 Academy of Sciences, 113, 10019-10024, 2016.
1104 Szutu, D. J. and Papuga, S. A.: Year-Round Transpiration Dynamics Linked With Deep Soil
1105 Moisture in a Warm Desert Shrubland, Water Resources Research, 0, 2019.
1106 Tabari, H., Martinez, C., Ezani, A., and Talaee, P. H.: Applicability of support vector machines
1107 and adaptive neurofuzzy inference system for modeling potato crop evapotranspiration,
1108 Irrigation science, 31, 575-588, 2013.
1109 Talsma, C., Good, S., Miralles, D., Fisher, J., Martens, B., Jimenez, C., and Purdy, A.: Sensitivity of
1110 Evapotranspiration Components in Remote Sensing-Based Models, Remote Sensing, 10, 1601,
1111 2018a.

1112   Talsma, C. J., Good, S. P., Jimenez, C., Martens, B., Fisher, J. B., Miralles, D. G., McCabe, M. F.,
1113   and Purdy, A. J.: Partitioning of evapotranspiration in remote sensing-based models,
1114   Agricultural and Forest Meteorology, 260-261, 131-143, 2018b.
1115   Tian, H., Chen, G., Liu, M., Zhang, C., Sun, G., Lu, C., Xu, X., Ren, W., Pan, S., and Chappelka, A.:
1116   Model estimates of net primary productivity, evapotranspiration, and water use efficiency in
1117   the terrestrial ecosystems of the southern United States during 1895–2007, Forest ecology and
1118   management, 259, 1311-1327, 2010.
1119   Trenberth, K. E., Fasullo, J. T., and Kiehl, J.: Earth's global energy budget, Bulletin of the
1120   American Meteorological Society, 90, 311-324, 2009.
1121   Vinukollu, R. K., Meynadier, R., Sheffield, J., and Wood, E. F.: Multi‐model, multi‐sensor
1122   estimates of global evapotranspiration: Climatology, uncertainties and trends, Hydrological
1123   Processes, 25, 3993-4010, 2011a.
1124   Vinukollu, R. K., Wood, E. F., Ferguson, C. R., and Fisher, J. B.: Global estimates of
1125   evapotranspiration for climate studies using multi-sensor remote sensing data: Evaluation of
1126   three process-based approaches, Remote Sensing of Environment, 115, 801-823, 2011b.
1127   Wang, K. and Dickinson, R. E.: A review of global terrestrial evapotranspiration: Observation,
1128   modeling, climatology, and climatic variability, Reviews of Geophysics, 50, 2012.
1129   Wang, K., Dickinson, R. E., Wild, M., and Liang, S.: Evidence for decadal variation in global
1130   terrestrial evapotranspiration between 1982 and 2002: 1. Model development, Journal of
1131   Geophysical Research: Atmospheres, 115, D20112, 2010.
1132   Wartenburger, R., Seneviratne, S. I., Hirschi, M., Chang, J., Ciais, P., Deryng, D., Elliott, J.,
1133   Folberth, C., Gosling, S. N., and Gudmundsson, L.: Evapotranspiration simulations in ISIMIP2a-
1134   Evaluation of spatio-temporal characteristics with a comprehensive ensemble of independent
1135   datasets, Environmental Research Letters, 13, 075001, 2018.
1136   Willett, K. M., Gillett, N. P., Jones, P. D., and Thorne, P. W.: Attribution of observed surface
1137   humidity changes to human influence, Nature, 449, 710, 2007.
1138   Xu, D., Agee, E., Wang, J., and Ivanov, V. Y.: Estimation of Evapotranspiration of Amazon
1139   Rainforest Using the Maximum Entropy Production Method, Geophysical Research Letters, 0,
1140   2019.
1141   Xu, T., Guo, Z., Liu, S., He, X., Meng, Y., Xu, Z., Xia, Y., Xiao, J., Zhang, Y., Ma, Y., and Song, L.:
1142   Evaluating Different Machine Learning Methods for Upscaling Evapotranspiration from Flux
1143   Towers to the Regional Scale, Journal of Geophysical Research: Atmospheres, 123, 8674-8690,
1144   2018.
1145   Yao, Y., Liang, S., Cheng, J., Liu, S., Fisher, J. B., Zhang, X., Jia, K., Zhao, X., Qin, Q., and Zhao, B.:
1146   MODIS-driven estimation of terrestrial latent heat flux in China based on a modified Priestley–
1147   Taylor algorithm, Agricultural and Forest Meteorology, 171, 187-202, 2013.
1148   Yao, Y., Liang, S., Li, X., Chen, J., Liu, S., Jia, K., Zhang, X., Xiao, Z., Fisher, J. B., and Mu, Q.:
1149   Improving global terrestrial evapotranspiration estimation using support vector machine by
1150   integrating three process-based algorithms, Agricultural and forest meteorology, 242, 55-74,
1151   2017.
1152   Yao, Y., Liang, S., Li, X., Liu, S., Chen, J., Zhang, X., Jia, K., Jiang, B., Xie, X., and Munier, S.:
1153   Assessment and simulation of global terrestrial latent heat flux by synthesis of CMIP5 climate
1154   models and surface eddy covariance observations, Agricultural and forest meteorology, 223,
1155   151-167, 2016.

Yuan, W., Liu, S., Liu, H., Randerson, J. T., Yu, G., and Tieszen, L. L.: Impacts of precipitation seasonality and ecosystem types on evapotranspiration in the Yukon River Basin, Alaska, Water Resources Research, 46, 2010.

Yue, S., Pilon, P., and Cavadias, G.: Power of the Mann–Kendall and Spearman's rho tests for detecting monotonic trends in hydrological series, Journal of hydrology, 259, 254-271, 2002.

Zaehle, S. and Friend, A.: Carbon and nitrogen cycle dynamics in the O‐CN land surface model: 1. Model description, site‐scale evaluation, and sensitivity to parameter estimates, Global Biogeochemical Cycles, 24, 2010.

Zeng, Z., Peng, L., and Piao, S.: Response of terrestrial evapotranspiration to Earth's greening, Current Opinion in Environmental Sustainability, 33, 9-25, 2018a.

Zeng, Z., Piao, S., Li, L. Z., Wang, T., Ciais, P., Lian, X., Yang, Y., Mao, J., Shi, X., and Myneni, R. B.: Impact of Earth greening on the terrestrial water cycle, Journal of Climate, 31, 2633-2650, 2018b.

Zeng, Z., Piao, S., Lin, X., Yin, G., Peng, S., Ciais, P., and Myneni, R. B.: Global evapotranspiration over the past three decades: estimation based on the water balance equation combined with empirical models, Environmental Research Letters, 7, 014026, 2012.

Zeng, Z., Wang, T., Zhou, F., Ciais, P., Mao, J., Shi, X., and Piao, S.: A worldwide analysis of spatiotemporal changes in water balance‐based evapotranspiration from 1982 to 2009, Journal of Geophysical Research: Atmospheres, 119, 1186-1202, 2014.

Zeng, Z., Zhu, Z., Lian, X., Li, L. Z., Chen, A., He, X., and Piao, S.: Responses of land evapotranspiration to Earth's greening in CMIP5 Earth System Models, Environmental Research Letters, 11, 104006, 2016.

Zhang, K., Kimball, J. S., Nemani, R. R., and Running, S. W.: A continuous satellite‐derived global record of land surface evapotranspiration from 1983 to 2006, Water Resources Research, 46, 2010.

Zhang, K., Kimball, J. S., Nemani, R. R., Running, S. W., Hong, Y., Gourley, J. J., and Yu, Z.: Vegetation greening and climate change promote multidecadal rises of global land evapotranspiration, Scientific reports, 5, 15956, 2015.

Zhang, K., Kimball, J. S., and Running, S. W.: A review of remote sensing based actual evapotranspiration estimation, Wiley Interdisciplinary Reviews: Water, 3, 834-853, 2016a.

Zhang, L., Lei, H., Shen, H., Cong, Z., Yang, D., and Liu, T.: Evaluating the Representation of Vegetation Phenology in the Community Land Model 4.5 in a Temperate Grassland, Journal of Geophysical Research: Biogeosciences, 124, 187-210, 2019.

Zhang, Y., Peña-Arancibia, J. L., McVicar, T. R., Chiew, F. H., Vaze, J., Liu, C., Lu, X., Zheng, H., Wang, Y., and Liu, Y. Y.: Multi-decadal trends in global terrestrial evapotranspiration and its components, Scientific reports, 6, 19124, 2016b.

Zhu, Z., Bi, J., Pan, Y., Ganguly, S., Anav, A., Xu, L., Samanta, A., Piao, S., Nemani, R. R., and Myneni, R. B.: Global data sets of vegetation leaf area index (LAI) 3g and Fraction of Photosynthetically Active Radiation (FPAR) 3g derived from Global Inventory Modeling and Mapping Studies (GIMMS) Normalized Difference Vegetation Index (NDVI3g) for the period 1981 to 2011, Remote Sensing, 5, 927-948, 2013.

1197   Zhu, Z., Piao, S., Myneni, R. B., Huang, M., Zeng, Z., Canadell, J. G., Ciais, P., Sitch, S.,
1198   Friedlingstein, P., and Arneth, A.: Greening of the Earth and its drivers, Nature Climate Change,
1199   2016. 2016.

1200   **Table 1.** Descriptions of models used in this study, including their drivers, adopted algorithms,

1201   key equations, limitations and references

Name	Input	Algorithm	Spatial resolution	Temporal resolution	Key equations	Limitations	References

Model	Input data	Method	Spatial resolution	Temporal resolution	Equation	Advantages/Limitations	Reference
MTE	Climate: precipitation, temperature, sunshine hour, relative humidity, wet days Vegetation: fAPAR	TRIAL ERROR	+0.5º×0.5º	Monthly	No specific equation	Insufficient flux observations in tropical regions; with no CO2 effect	Jung et al. (2011)
RF	enhanced vegetation index, fAPAR, leaf area index, land surface temperature, radiation, potential radiation, index of water availability, relative humidity	Randomized decision tree	0.5º×0.5º	Half-hourly	No specific equation	The same with MTE	Bodesheim et al. (2018)
P-LSH	Climate: radiation, air temperature, vapor pressure, wind speed, CO2 Vegetation: AVHRR NDVI	Modified Penman–Monteith	0.083 º×0.083º	Monthly	$E_v = \dfrac{\Delta R_n + \rho C_p VPD g_a}{\lambda_v(\Delta + \Upsilon(1 + \frac{g_a}{g_s}))}$ $E_s = RH^{\frac{VPD}{k}} \dfrac{\Delta R_n + \rho C_p VPD g_a}{\lambda_v(\Delta + \Upsilon(1 + \frac{g_a}{g_s}))}$	Advantages: more robust physical basis; consider the effects of CO$_2$ Limitations: high meteorological forcing requirements; canopy conductance is based on proxies;	Zhang et al. (2015)
GLEAM	Climate: precipitation, net radiation, surface soil moisture, land surface temperature, air temperature, snow depth Vegetation: vegetation optical depth	Modified Priestley–Taylor	0.25º×0.25º	Daily	$E_s = f_s S_s \alpha_s \dfrac{\Delta}{\lambda_v \rho_w(\Delta + \gamma)}(R_n^s - G_s)$ $E_{sc} = f_{sc} S_{sc} \alpha_{sc} \dfrac{\Delta}{\lambda_v \rho_w(\Delta + \gamma)}(R_n^{sc} - G_{sc})$ $E_{tc} = f_{tc} S_{tc} \alpha_{tc} \dfrac{\Delta}{\lambda_v \rho_w(\Delta + \gamma)}(R_n^{tc} - G_{tc}) - \beta E_i$	Advantages: simple; low requirement for meteorological data; well-suited for remote sensing observable variables; soil moisture is considered Limitations: many simplifications of physical processes; neither VPD nor surface and aerodynamic resistances are explicitly accounted for; strong dependency on net radiation	(Miralles et al., 2011)
MODIS	Climate: air temperature, shortwave radiation, wind speed, relative humidity, air pressure Vegetation: LAI, fAPAR, albedo	Penman–Monteith–Leuning	0.05 º×0.05 º	Monthly	$E_i = f_{wet} f_c \dfrac{\Delta(R_n - G) + \rho c_p \frac{VPD}{r_a^{wc}}}{\lambda_v \rho_w(\Delta + \gamma \frac{r_s^{wc}}{r_a^{wc}})}$ $E_v = (1 - f_{wet}) f_c \dfrac{\Delta(R_n - G) + \rho c_p \frac{VPD}{r_a^t}}{\lambda_v \rho_w(\Delta + \Upsilon \frac{r_s^t}{r_a^t})}$ $E_s = [f_{wet} + \dfrac{(1 - f_{wet})hVPD}{\beta}] \dfrac{(s A_{soil} + \frac{\rho c_p(1 - f_c)VPD}{r_{as}})}{\lambda_v \rho_w(S + \gamma \frac{r_{tot}}{r_{as}})}$	Advantages: more robust physical basis; Limitations: require many variables that are difficult to observe or not observable with satellites; canopy conductance is based on proxies; do not consider soil moisture but use atmospheric humidity as a surrogate; do not	Mu et al. (2011)

consider the effects of CO_2

Name	Algorithm	Spatial resolution	Temporal resolution	Key equations	Advantages/Limitations	References
PML-CSIRO	Climate: Penman–Monteith–Leuning precipitation, air temperature, vapor pressure, shortwave radiation, longwave radiation, wind speed Vegetation: AVHRR LAI, emissivity and albedo	0.5º×0.5º	Monthly	$$E_v = \frac{\Delta R_n + \rho C_p VPD g_a}{\lambda_v(\Delta + \Upsilon\left(1 + \frac{g_a}{g_s}\right))}$$ $$E_s = \frac{f\Delta A_s}{\Delta + \gamma}$$ E_i: an adapted version of Gash rainfall interception model (Van et al., 2001)	Advantages: more robust physical basis (compared to Priestley–Taylor equation); biophysically based estimation of surface conductance Limitations: high meteorological forcing requirements; canopy conductance is based on proxies; do not consider the effects of CO_2	Zhang et al. (2016b)

TRENDY LSMs

Advantages: land surface models are process-oriented and physically-based. Given their structure almost all models are capable to allow factorial analysis, where one forcing can be applied at a time. Most models also consider the physiological effect of CO_2 on stomatal closure.

Disadvantages: most models typically do not allow integration/assimilation of observation-based vegetation characteristics. Model parameterizations remain uncertain and a same process is modelled in different ways across models. Model parameters may or may not be physically-based and therefore measurable in the field.

Models participating in the TRENDYv6 comparison were forced by precipitation, air temperature, specific humidity, shortwave radiation, longwave radiation, wind speed based on the CRU-NCEPv8 data as explained in Le Quere et al. 2018. It is very difficult to list all key equations for all land surface models. Here, we just list the stomatal conductance equation for each model.

Name	Algorithm	Spatial resolution	Temporal resolution	Key equations	References
CABLE	Penman-Monteith	0.5º×0.5º	Monthly	$g_s = g_0 + \frac{g_1 f_w A}{c_a - c_p}(1 + \frac{VPD}{VPD_0})^{-1}$	Haverd et al. (2018)
CLASS-CTEM	Modified Penman–Monteith	2.8125º×2.8125º	Monthly	$g_c = m\frac{A_n p}{(c_s - \Gamma)}\frac{1}{(1 + VPD/VPD_0)} + b\,LAI$	Melton and Arora (2016)
CLM45	Modified Penman–Monteith	1.875º×2.5º	Monthly	$g_s = g_0 + \frac{g_1 A}{c_a}RH$	Oleson et al. (2010)
DLEM	Penman–Monteith	0.5º×0.5º	Monthly	$g_s = \max(g_{smax} r_{corr} bf(ppdf)f(T_{min})f(VPD)f(CO_2), g_{smin})$	Pan et al. (2015)
ISAM	Modified Penman–Monteith	0.5º×0.5º	Monthly	$g_s = m\frac{A}{C_s/P_{atm}} \times \frac{e_s}{e_i} + b_t \beta_t$	Barman et al. (2014)
JSBACH	Penman–Monteith	1.9º×1.9º	Monthly	$g_s = \beta_w \frac{1.6 A_{n,pot}}{c_a - c_{i,pot}}$	Knauer et al. (2015)
JULES	Penman–Monteith	2.5º×3.75º	Monthly	Bare soil conductance: $g_{soil} = \frac{1}{100}(\frac{\theta_1}{\theta_c})^2$ Stomatal conductance is calculated by solving the two equations: $A_l = g_s(C_s - C_i)/1.6$; $$\frac{C_i - \Gamma^*}{C_c - \Gamma^*} = f_0(1 - \frac{\Delta}{q_c})$$	Li et al. (2016)
LPJ-GUESS	Equations proposed by Monteith (1995)	0.5º×0.5º	Monthly	$g_s = g_{smin} + \frac{1.6 A_{dt}}{c_a(1 - \lambda_c)}$	Smith (2001)
LPJ-wsl	Priestley-Taylor	0.5º×0.5º	Monthly	$g_s = g_{smin} + \frac{1.6 A_{dt}}{c_a(1 - \lambda_c)}$	Sitch et al. (2003)
LPX-Bern	Modified equation of Monteith (1995)	1º×1º	Monthly	$g_s = g_{smin} + \frac{1.6 A_{dt}}{c_a(1 - \lambda_c)}$	Keller et al. (2017)
O-CN	Modified Penman-Monteith	1º×1º	Monthly	$g_s = g_{smin} + \frac{1.6 A_{dt}}{c_a(1 - \lambda_c)}$	Zaehle and Friend (2010)

ORCHID EE	Modified Penman-Monteith	0.5°×0.5°	Monthly	$g_s = g_0 + \dfrac{A + R_d}{c_a - c_p} f_{vpd}$ $g_{soil} = \exp(8.206 - 4.255 W/W_{sat})$	d'Orgeval et al. (2008)
ORCHID EE-MICT	Modified Penman-Monteith	0.5°×0.5°	Monthly	$g_s = g_0 + \dfrac{A + R_d}{c_a - c_p} f_{vpd}$	Guimberteau et al. (2018)
VISIT	Penman–Monteith	0.5°×0.5°	Monthly	$g_s = g_0 + \dfrac{g_1 f_w A}{c_a - c_p}(1 + \dfrac{VPD}{VPD_0})^{-1}$	Ito (2010)

Notes: A: net assimilation rate; A_{dt}: total daytime net photosynthesis; $A_{n,pot}$: unstressed net assimilation rate; b: soil moisture factor; b_t: stomatal conductance intercept; c_a: atmospheric CO_2 concentration; c_c: critical CO_2 concentration; c_i: internal leaf concentration of CO_2; $c_{i,\,pot}$: internal leaf concentration of CO_2 for unstressed conditions; c_s: leaf surface CO_2 concentration; c_p: CO_2 compensation point; e_s: vapor pressure at leaf surface; e_i: saturation vapor pressure inside the leaf; E_s: soil evaporation; E_c: canopy evapotranspiration; E_{dry}: dry canopy evapotranspiration; E_{wet}: wet canopy evapotranspiration; E_v: canopy transpiration; E_i: canopy interception; E_{tc}: transpiration from tall canopy; E_{sc}: transpiration from short canopy; f: fraction of *P* to equilibrium soil evaporation; f_s: soil fraction; f_{sc}: short canopy fraction; f_{tc}: tall canopy fraction; f_{vpd}: factor of the effect of leaf-to-air vapor pressure difference; f_w: a function describing the soil water stress on stomatal conductance; f_{wet}: relative surface wetness parameter; f_0: the maximum ratio of internal to external CO_2; *f(ppdf)*:limiting factor of photosynthetic photo flux density; *f(T_min)*: limiting factor of daily minimum temperature; *f(VPD)*: limiting factor of vapor pressure deficit; *f(CO_2)*: limiting factor of carbon dioxide; G: ground energy flux; g_a: aerodynamic conductance; g_m: empiricalparameter; g_s: stomatal conductance; g_{smax}: maximum stomatal conductance; g_{smin}: minimum stomatal conductance; g_{soil}: bare soil conductance; g_0: residual stomatal conductance when the net assimilation rate is 0 ; g_1: sensitivity of stomatal conductance to assimilation, ambient CO_2 concentration and environmental controls; I: tall canopy interception loss; m: stomatal conductance slope; P_{atm}: atmospheric pressure; PE_s: potential soil evaporation; PE_{canopy}: potential canopy evaporation; q_a: specific air humidity; q_c: critical humidity deficit; q_s: specific humidity of saturated air; r_a: aerodynamic resistance; r_s: stomatal resistance; R_n: net radiation; Rd: day respiration; RH: relative humidity; T_s: actual surface temperature; VPD: vapor pressure deficit; VPD_0: the sensitivity of stomatal conductance to VPD; W: top soil moisture; W_{canopy}: canopy water; W_{sat}: soil porosity; α: Priestley-Taylor coefficient; $α_m$: empirical parameter; *β:* a constant accounting for the times in which vegetation is wet; $β_t$: soil water availability factor between 0 and 1; $β_w$: A scaling factor to account for water stress; $β_s$: moisture availability function; ρ: air density; γ: psychrometric constant; $λ_v$: latent heat of vaporization; $λ_c$: ratio of intercellular to ambient partial pressure of CO_2; r_{corr}: correction factor of temperature and air pressure on conductance; $Γ^*$: CO_2 compensation point when leaf day respiration is zero; $θ_1$: parameter of moisture concentration in the top soil layer; $θ_c$: parameter of moisture concentration in the spatially varying critical soil moisture; Δ: slope of the vapor pressure curve.

1233 **Table 2**. Inter-annual variability (IAV, denoted as standard deviation) and trend of global

1234 terrestrial ET during 1982-2011 and the contribution of vegetation greening to ET trend. * suggests

1235 significance of the trend at the 95% confidence level ($p<0.05$).

	Model	ET IAV (mm yr^{-1})	ET Trend (mm yr^{-2})	Greening-induced ET change (mm yr^{-2})	Sensitivity of ET to LAI (mm yr^{-2} per m^2 m^{-2})	LAI trend (10^{-3} m^2 m^{-2} yr^{-1})
Machine learning	MTE	5.93	0.38*	0.09	35.86	2.51*
RS models	P-LSH	9.95	1.07*	0.34	135.46	2.51*
	GLEAM	8.47	0.33*	0.14	55.78	2.51*
	PML-CSIRO	7.18	0.41*	0.36	143.43	2.51*
	RS model mean	7.98	0.62*	0.28	111.55	2.51*
LSMs	CABLE	9.63	0.07	0.35	102.64	3.41*
	CLASS-CTEM	12.22	0.35*	0.53	134.52	3.94*
	CLM45	8.68	0.38*	0.31	67.54	4.59*
	DLEM	7.21	0.26*	0.53	200.76	2.64*
	ISAM	7.50	0.22	0.16	32.26	4.96*
	JSBACH	10.12	-0.05	0.50	217.39	2.30*
	JULES	11.33	-0.02	0.34	85.21	3.99*
	LPJ-GUESS	7.48	0.50*	0.28	160.92	1.74*
	LPJ-wsl	4.77	0.24*	0.19	31.56	6.02*
	LXP-Bern	4.80	0.20*	0.04	4.04	9.90*
	O-CN	10.41	0.32*	0.53	89.23	5.94*
	ORCHIDEE	9.28	-0.17	0.21	96.33	2.18*
	ORCHIDEE-MICT	10.70	-0.34*	0.50	171.23	2.92*
	VISIT	6.31	0.87*	0.70	51.40	13.62*
	LSM mean	7.73	0.23	0.37	79.91	4.63*

1236